CSF1R+ macrophage and osteoclast depletion impairs neural crest proliferation and craniofacial morphogenesis

Felix Ma[1,2], Rose Ru Jing Zhou[2,3], Matthew Rosin[2,4], Iris Zhou[2,3,#], Sabrina Ownsworth[2,3,#], Rouzbeh Ostadsharif Memar[1,2,5], Vincent B. Wong[2,6], Jessica M. Rosin[2,4,7,*]

[1]Craniofacial Science Graduate Program, Faculty of Dentistry, The University of British Columbia, Vancouver, BC V6T 1Z3, Canada
[2]Life Sciences Institute, The University of British Columbia, Vancouver, BC V6T 1Z3, Canada
[3]Doctor of Dental Medicine Program, Faculty of Dentistry, The University of British Columbia, Vancouver, BC V6T 1Z3, Canada
[4]Department of Oral Biological and Medical Sciences, Faculty of Dentistry, The University of British Columbia, Vancouver, BC V6T 1Z3, Canada
[5]Division of Periodontics and Dental Hygiene, Faculty of Dentistry, The University of British Columbia, Vancouver, BC V6T 1Z3, Canada
[6]Neuroscience Program, Faculty of Science, McGill University, Montreal, QC H3A 1A1, Canada
[#]Authors contributed equally
[7]Lead contact
*Correspondence: jessica.rosin@ubc.ca

SUMMARY

Despite a wealth of knowledge on the mechanisms underlying craniofacial morphogenesis during gestation, the roles of fetal macrophages and osteoclasts during this process remain less well characterized. Here, we used the pharmacological inhibitor PLX5622 to disrupt colony stimulating factor-1 receptor (CSF1R) signaling, which is essential for macrophage and osteoclast proliferation, differentiation, and survival. Prenatal PLX5622 exposure resulted in ~50% depletion of CSF1R+ macrophages, with complete loss of osteoclasts. While there were no notable changes in craniofacial nerve or muscle development, prenatal exposure to PLX5622 resulted in skull doming and cranial suture impairments, in addition to disruptions to development of the premaxilla, mandible, ear ossicles, palate, and cranial base. In response to PLX5622 exposure, cytokine and chemokine signaling was altered and neural crest proliferation was impaired. Our data also highlight sex- and strain-specific differences in PLX5622

phenotypes and together demonstrate that CSF1R+ macrophages and osteoclasts are essential for craniofacial morphogenesis.

KEYWORDS

macrophage, osteoclast, neural crest, nerve, muscle, cartilage, bone, embryogenesis, craniofacial morphogenesis, colony stimulating factor-1 receptor (CSF1R)

INTRODUCTION

Colony stimulating factor-1 receptor (CSF1R) is expressed in cells of the mononuclear phagocyte lineage—namely microglia, macrophages, and osteoclasts—and is required for their proliferation, survival, and differentiation[1-6]. CSF1R binds to two ligands, colony stimulating factor-1 (CSF1) and interleukin-34 (IL-34), which stimulate proliferative and differentiating signals via STAT, AKT, and ERK1/2 pathways[2,3,7]. CSF1R is essential for phagocytic and bone resorptive functions in macrophages and osteoclasts, respectively[6,8]. Deficient CSF1R signaling in rodents has been shown to cause an osteopetrotic phenotype, where a lack of CSF1R+ cells leads to disruption of bone marrow cavities, loss of bone marrow hematopoiesis, and increased bone density[9-12]. The *osteopetrotic* (*op*) phenotype has been characterized in *Csf1*$^{op/op}$ ligand mutant mice and *Csf1r* knockout (KO) mice[9,10,13,14]. These mice have reduced litter sizes and early postnatal lethality (up to 100%) depending on the strain[9,10,14]. Phenotypes observed in both *Csf1/Csf1r*-disrupted mouse models also include a domed skull, shortened snout, and toothlessness, while an osteosclerotic otic capsule, incus, and stapes have only been observed in *Csf1*$^{op/op}$ mice[10,15,16]. At the cellular level, these mice are deficient in blood monocytes and macrophages in most tissues; microglia are depleted in the receptor knockout but unaffected in

57 the ligand mutant[9,14,17-19]. The *Csf1 toothless* (*tl*) rat and *Csf1r* KO rat closely replicate the mouse
58 phenotypes, including osteopetrosis, doming of the skull, a shortened snout, toothlessness, and
59 microglia and macrophage depletion across most tissues[11,12]. Interestingly, *Csf1r* KO rats also
60 present with additional phenotypes such as hypomineralization of the calvaria, impairment of the
61 cranial sutures, bulging eyes, and sclerosis of the cranial base[11,20-22]. Viability is markedly
62 improved in rat models, with only 23% of males dying postnatally and all females surviving
63 beyond weaning[11]. In humans, bi-allelic *CSF1R* mutations can cause bone phenotypes such as
64 osteosclerosis of the cranial vault and cranial base, in addition to narrowing of the optic
65 canal[23,24].
66
67 To study the role of CSF1R+ cells in mediating the above-mentioned phenotypes, we previously
68 reported a pharmacological inhibition model for disrupting these cells in a temporally-controlled
69 manner, focusing on embryogenesis[25,26]. The CSF1R inhibitor PLX5622 was fed via chow to
70 pregnant CD1 mice from embryonic day 3.5 (E3.5) onwards to expose mouse embryos to the
71 inhibitor[25]. Indeed, like the severe depletion of microglia in the *Csf1r* KO mouse, treatment with
72 PLX5622 depleted ~99% of microglia in the hypothalamus by E15.5, demonstrating excellent
73 oral bioavailability, penetrance, and efficacy of this model[25]. Outside of the brain, PLX5622
74 exposure was found to cause a noticeable reduction in CSF1R+ cells throughout craniofacial
75 tissues at E18.5[26]. As in the mutant mouse models described, PLX5622 treatment also reduced
76 litter sizes and increased postnatal lethality (~23%)[25]. These CD1 mice also presented with
77 domed skulls in addition to morphological disruptions to the incisors and molars; although, the
78 continuous eruption of incisors did not appear to be inhibited[25]. Using Geometric Morphometric
79 (GM) analyses, craniofacial and mandibular shape and size were shown to be significantly

80 changed and decreased, respectively, by PLX5622 exposure[26]. Interestingly, a recent study
81 showed that intragastric administration of PLX5622 to pregnant ICR mice between E14.5-17.5
82 reduced osteoclasts and resulted in an enlarged cartilaginous zone in the midpalatal suture[27].
83 However, previous studies did not fully characterize the depletion of CSF1R+ cells outside of the
84 brain or across embryogenesis, nor did they thoroughly describe all craniofacial phenotypes or
85 identify the underlying morphogenetic disruptions leading to the phenotypes observed using this
86 pharmacological inhibition model.
87
88 In this study, we used our previously established pharmacological inhibition model to study the
89 impact of prenatal PLX5622 exposure on craniofacial nerve, muscle, cartilage, and bone
90 development across embryogenesis in two strains (CD1 & C57BL/6) and both sexes (males &
91 females). Exposure to PLX5622 resulted in a continuous and stable depletion of CSF1R+
92 macrophages to ~50% across gestation, in addition to the complete loss of osteoclasts. Although
93 we did not observe overt changes in craniofacial nerve or muscle development across
94 embryogenesis, disrupted bone phenotypes in craniofacial tissue of PLX5622-exposed animals
95 could be observed as early as E15.5, with notable abnormalities in skull shape, cranial sutures,
96 ear ossicles, premaxilla, mandible, palate, and cranial base observed by birth. We identified
97 significant alterations in the secretion of 18 cytokine and chemokines from cultured craniofacial
98 tissues in response to prenatal PLX5622 exposure and validated that several such secreted factors
99 are indeed expressed by CSF1R+ macrophages. At the cellular level, exposure to PLX5622
100 across gestation decreased neural crest cell (NCC) proliferation both *in vitro* in a sphere assay
101 and *in vivo* in embryonic craniofacial tissue cryosections, resulting in fewer NCCs in tissues
102 impacted by PLX5622 exposure. Together, these data demonstrate that CSF1R+ macrophages

103 and osteoclasts are required for craniofacial morphogenesis during the embryonic period, and
104 suggest that altered signaling to NCCs may underlie the phenotypes observed in PLX5622
105 offspring.
106
107 **RESULTS**
108 **Embryonic Exposure to the CSF1R Inhibitor PLX5622 Depletes CSF1R+ Macrophages and**
109 **Osteoclasts**
110 As gestational exposure to the CSF1R inhibitor PLX5622 dramatically reduces embryonic
111 microglial populations by ~99%[25], and CSF1R function is essential for macrophage and
112 osteoclast proliferation, differentiation, and survival[5,6], we tested the impact of PLX5622 on
113 reducing macrophage and osteoclast populations in craniofacial tissues across embryogenesis. As
114 previously described[25], pregnant dams were fed control or PLX5622 diet starting at E3.5 to avoid
115 disrupting embryo implantation, which is regulated by endometrial macrophages[28,29].
116 Craniofacial tissues were collected for flow cytometry from E11.5, 13.5, 15.5, and 17.5 male and
117 female *Csf1r*^{EGFP} transgenic embryos exposed to control or PLX5622 diet (Figures 1A-1B).
118 Quantification of *Csf1r*$^{EGFP+}$ cells revealed a significant decrease by E11.5, with only 42.7% of
119 *Csf1r*$^{EGFP+}$ cells remaining in PLX5622 embryos compared to controls (Figure 1B; p=0.0003).
120 Similarly, by E13.5, *Csf1r*$^{EGFP+}$ cells were noticeably depleted in PLX5622 craniofacial tissues
121 compared to controls, with only 65.1% of *Csf1r*$^{EGFP+}$ cells remaining (Figure 1B; p<0.0001).
122 *Csf1r*$^{EGFP+}$ cells depletion was sustained across E15.5 and E17.5, with only 61.8% and 45.2% of
123 *Csf1r*$^{EGFP+}$ cells, respectively, remaining in PLX5622 craniofacial tissues compared to control
124 (Figure 1B; E15.5 p<0.0001, E17.5 p<0.0001). Administering PLX5622 gestationally did not
125 significantly impact embryonic litter size (Table S1; CD1 p=0.0698, C57BL/6 p=0.5683), the

126 number of embryo resorptions per litter (Table S1; CD1 p=0.6110, C57BL/6 p=0.4176), or
127 embryo sex ratios (Table S1; CD1 p=0.5676, C57BL/6 p=0.4612) in CD1 or C57BL/6 mice.
128
129 To visualize and quantify tissue-specific depletion of CSF1R-expressing cells within the embryo,
130 craniofacial tissue cryosections were collected from E15.5 male and female *Csf1r*^{EGFP} transgenic
131 embryos and stained with a CSF1R antibody. *Csf1r*^{EGFP} fluorescence and CSF1R staining
132 revealed a noticeable decrease in the number of CSF1R-expressing cells in and around several
133 developing craniofacial structures of E15.5 PLX5622 embryos as compared to controls (Figures
134 1C–1W). Specifically, CSF1R-expressing cells were significantly depleted in and around
135 developing cartilaginous and/or bony structures of PLX5622 embryos, with only 53.1% of
136 *Csf1r*$^{EGFP+}$ and 32.3% of CSF1R+ cells remaining around the nasal septum (Figures 1C–1E,
137 arrows; *Csf1r*^{EGFP} p=0.0003, CSF1R p=0.0001), 36.5% of *Csf1r*$^{EGFP+}$ and 23.9% of CSF1R+
138 cells remaining around Meckel's cartilage (Figures 1F–1H, arrows; *Csf1r*^{EGFP} p<0.0001; CSF1R
139 p<0.0001), and 31.9% of *Csf1r*$^{EGFP+}$ and 21.7% of CSF1R+ cells remaining in the ear (Figures
140 1I–1K, arrows; *Csf1r*^{EGFP} p<0.0001, CSF1R p<0.0001). The maxillary incisor was an exception,
141 where no significant difference was observed between E15.5 controls and PLX5622 embryos
142 (Figures 1L–1N, arrows; *Csf1r*^{EGFP} p=0.0698, CSF1R p=0.0707). CSF1R-expressing cells were
143 also significantly reduced in craniofacial nervous tissue of PLX5622 embryos, with only 39.7%
144 of *Csf1r*$^{EGFP+}$ and 21.7% of CSF1R+ cells remaining in the eye (Figures 1O–1Q, arrows;
145 *Csf1r*^{EGFP} p=0.0002, CSF1R p=0.0001), and 56.7% of *Csf1r*$^{EGFP+}$ and 43.1% of CSF1R+ cells
146 remaining in the trigeminal (Figures 1R–1T, arrows; *Csf1r*^{EGFP} p=0.0005, CSF1R p=0.0013).
147 Moreover, CSF1R-expressing cells were also significantly reduced in muscle tissue, with only
148 48.9% of *Csf1r*$^{EGFP+}$ and 27.4% of CSF1R+ cells remaining in the tongue of E15.5 PLX5622

149 embryos as compared to controls (Figures 1U–1W, arrows; *Csf1r*^{EGFP} p=0.0002, CSF1R
150 p<0.0001).
151
152 While visualizing E15.5 male and female *Csf1r*^{EGFP} craniofacial tissue sections using high-
153 resolution confocal microscopy, we observed multinucleated *Csf1r*$^{EGFP+}$ cells within several
154 craniofacial bones such as the premaxilla, maxilla, and mandible (Figures 2A-2F', arrows). To
155 quantify osteoclast-specific depletion following gestational exposure to PLX5622, we labelled
156 osteoclasts with a Cathepsin K (CTSK) antibody. Intriguingly, exposure to PLX5622 completely
157 depleted CTSK+/*Csf1r*$^{EGFP+}$ double-positive multinucleated osteoclasts in the E15.5 mandible
158 (Figures 2E–2I, arrows; p=0.0007). Moreover, there was a complete loss of all single-positive
159 *Csf1r*$^{EGFP+}$ multinucleated cells in the E15.5 PLX5622 mandible as compared to control (Figures
160 2E–2I; p<0.0001). As embryonic osteoclasts appeared to be absent in the E15.5 mandible of
161 PLX5622 embryos when compared to controls, we then looked to determine whether this led to
162 loss of bone resorptive function across the embryonic head. Tartrate-resistant acid phosphatase
163 (TRAP) staining of E15.5 craniofacial tissues revealed loss of osteoclastic activity surrounding
164 developing craniofacial bones, including the mandible, maxilla, frontal, basioccipital, and
165 exoccipital bones (Figures 2J–2S', arrows). Together, the data demonstrate that exposure to the
166 CSF1R inhibitor PLX5622 during gestation significantly depletes CSF1R-expressing cells across
167 embryogenesis and disrupts osteoclast development and activity. These findings were observed
168 in both male and female embryos.
169
170 **CSF1R+ Cell Depletion Results in Tissue-Specific Changes in Apoptosis in the Developing**
171 **Embryo**

172 Considering that one of the main functions of macrophages is to phagocytose apoptotic cells and
173 cellular debris[30,31], and apoptosis is an essential process in embryonic craniofacial
174 development[32-35], craniofacial tissue cryosections collected from E15.5 male and female
175 *Csf1r*^{EGFP} transgenic embryos were stained with an active cleaved Caspase 3 (CC3) antibody to
176 visualize whether apoptotic cells accumulated following CSF1R+ cell depletion. We were also
177 interested in whether we would observe CC3+/*Csf1r*$^{EGFP+}$ double-positive cells, as the reduction
178 in CSF1R+ cells should be mediated in part by cell death. Interestingly, no changes in CC3+
179 single-positive or CC3+/*Csf1r*$^{EGFP+}$ double-positive cells were observed surrounding the E15.5
180 nasal septum (Figures S1A–S1C, arrows; CC3 p=0.0956, CC3/*Csf1r*^{EGFP} p=0.3654) or Meckel's
181 cartilage (Figures S1D–S1F, arrows; CC3 p=0.8888, CC3/*Csf1r*^{EGFP} p=0.1774) when comparing
182 PLX5622 to control. In contrast, there was a significant increase in CC3+ single- and
183 CC3+/*Csf1r*$^{EGFP+}$ double-positive cells in the E15.5 PLX5622 ear (Figures S1G–S1I, arrows;
184 CC3 p=0.0317, CC3/*Csf1r*^{EGFP} p=0.0145). No change in CC3+ single-positive cells was found
185 surrounding the E15.5 maxillary incisor (Figures S1J–S1L, arrows; CC3 p=0.6109); moreover,
186 no CC3+/*Csf1r*$^{EGFP+}$ double-positive cells could be observed surrounding the maxillary incisor
187 in either control or PLX5622 embryos (Figures S1J–S1L). Outside of developing
188 cartilaginous/bony structures, CC3+ single-positive cells accumulated in nervous and muscle
189 tissues following PLX5622 exposure, particularly in the eye (Figures S1M–S1O, arrows; CC3
190 p=0.0065), trigeminal (Figures S1P–S1R, arrows; CC3 p=0.0025), and tongue (Figures S1S–
191 S1U, arrows; CC3 p<0.0001). However, a significant increase in the number of CC3+/*Csf1r*$^{EGFP+}$
192 double-positive cells was only observed in the eye of E15.5 PLX5622 embryos (Figure S1O;
193 CC3/*Csf1r*^{EGFP} p=0.0208), with no change observed in the trigeminal (Figure S1R;
194 CC3/*Csf1r*^{EGFP} p=0.2959) or tongue (Figure S1U; CC3/*Csf1r*^{EGFP} p=0.5995). Collectively, the

195 data suggests that depleting CSF1R+ cells during embryogenesis leads to an accumulation of
196 apoptotic cells in both male and female craniofacial tissues. Increases in cell death were
197 predominantly observed in nervous and muscular structures, but not in or around developing
198 cartilaginous/bony structures, except for the ear.
199

200 **Embryonic Exposure to the CSF1R Inhibitor PLX5622 Does Not Impact Craniofacial Nerve**
201 **or Muscle Development**

202 In this study, we sought to thoroughly characterize the craniofacial phenotypes resulting from
203 embryonic PLX5622 exposure, especially as embryonic soft tissues were previously unexplored
204 in *Csf1*/*Csf1r*-disrupted genetic models[9-12,14,15,21] and our own pharmacological model using
205 PLX5622[25,26]. Accordingly, we first examined craniofacial nerve development from E11.5 to
206 E13.5 using a Neurofilament antibody (2H3) and whole-mount immunostaining (Figure S2).
207 Neurofilament staining in the trigeminal and facial nerves, including the zygomatic, buccal, and
208 marginal branches of the trigeminal, were comparable between E11.5 control and PLX5622 male
209 and female CD1 (Figures S2A-S2D) and C57BL/6 (data not shown) embryos. Similarly,
210 neurofilament staining in the facial nerve, auriculotemporal nerve, and great auricular nerve were
211 comparable between E12.5 control and PLX5622 male and female CD1 (Figures S2E-S2H) and
212 C57BL/6 (data not shown) embryos. Moreover, craniofacial nerve development continued to be
213 comparable at E13.5, whereby the great auricular nerve, auriculotemporal nerve, zygomatic
214 branch of the trigeminal, superior buccolabial nerve, inferior buccolabial nerve, and marginal
215 mandibular nerve appeared similar between control and PLX5622 male and female CD1 (Figures
216 S2I-S2L) and C57BL/6 (data not shown) embryos.
217

218 Next, we examined craniofacial muscle development from E11.5 to E13.5 using a Myosin Heavy
219 Chain antibody (MF 20) and whole-mount immunostaining (Figure S3). Muscle staining in the
220 masseter, auricularis, buccinator, and zygomaticomandibularis, appeared comparable across
221 E11.5 to E13.5 in control and PLX5622 male and female CD1 embryos (Figures S3A-S3L). To
222 assess the development of muscles deeper in the tissues, immunofluorescence staining was
223 performed on E15.5 craniofacial tissue cryosections using the MF20 antibody (Figure S4).
224 Muscle fiber diameter and density appeared comparable in the buccinator, deep masseter and
225 zygomaticomandibularis, superficial masseter, temporalis and pterygoid, tongue, and extraocular
226 muscles, including the superior oblique, inferior oblique, superior rectus, medial rectus, inferior
227 rectus, and retractor bulbi between E15.5 control and PLX5622 male and female C57BL/6
228 embryos (Figures S4A-S4L'). As a whole, the data suggests that depleting CSF1R+ cells during
229 embryogenesis does not noticeably impact the gross morphology of craniofacial nerves or
230 muscles in male or female CD1 or C57BL/6 embryos.
231
232 **Embryonic Exposure to the CSF1R Inhibitor PLX5622 Drives Sex, Strain, and Time-**
233 **Dependent Disruptions to Craniofacial Bone Morphogenesis**
234 Previously, we reported doming of the cranial vault, mandibular disruptions, and dental
235 phenotypes in P21 and P28 CD1 mice exposed to PLX5622 embryonically[25,26]. However, our
236 prior analyses did not fully characterize all of the cartilaginous and/or bony phenotypes present
237 in PLX5622 offspring. Moreover, the *Csf1*/*Csf1r*-disrupted genetic models and our own
238 pharmacological PLX5622 studies failed to examine craniofacial morphogenesis during the
239 embryonic period[9-12,15,16,21,25,26]. As we observed a loss of osteoclasts and bone resorptive activity
240 in E15.5 PLX5622 embryos in the current study (see Figure 2), we utilized E15.5 craniofacial

241 tissue cryosections to visualize the impact of PLX5622 exposure on osteoblasts and bone
242 formation during embryogenesis. To start, immunofluorescence staining with an Sp7 antibody
243 was performed to label osteoblasts. Disrupted patterning in the premaxilla and mandible (Figures
244 3A–3D', arrows) was observed in E15.5 male and female PLX5622 embryos, while other
245 craniofacial bones such as the maxilla, frontal bone, and basioccipital bone (Figures 3E-3J')
246 displayed comparable Sp7 staining between E15.5 control and PLX5622 male and female
247 embryos.
248
249 Next, we evaluated cartilage and bone development using Alcian blue and von Kossa staining,
250 respectively. Craniofacial cartilage development appeared unimpacted, as Alcian blue staining
251 was comparable between E15.5 control and PLX5622 male and female embryos (Figures 3K-
252 3T'). In contrast, increased bone density in the premaxilla and mandible (Figures 3K–3N',
253 arrows) was observed in E15.5 male and female PLX5622 embryos, which complemented the
254 altered osteoblast patterning observed in these bones. Moreover, consistent with Sp7 osteoblast
255 staining, bone density in other craniofacial bones such as the maxilla, frontal bone, and
256 basioccipital bone (Figures 3O-3T') appeared comparable between E15.5 control and PLX5622
257 male and female embryos.
258
259 To investigate if the changes in osteoblast/bone development in PLX5622 embryos begin prior to
260 E15.5, micromass cultures of mesenchymal cells collected from the frontonasal mass (gives rise
261 to premaxilla)[36-38] and mandible of E12.5 control and PLX5622 male and female embryos were
262 stained for alkaline phosphatase activity as a readout for bone mineralization. Relative to total
263 micromass area, which was stained with hematoxylin, control and PLX5622 frontonasal mass-

264 derived micromass cultures did not show a significant difference in alkaline phosphatase staining
265 (Figures 4A–4F; p=0.7043), while mandible-derived micromass cultures showed a non-
266 significant increase in alkaline phosphatase staining upon PLX5622 exposure (Figures 4G–4L;
267 p=0.0680).
268
269 Although our findings suggest a possible increase in osteoblast differentiation and/or osteogenic
270 potential in the premaxilla and mandible of PLX5622 embryos between E12.5 and E15.5, we
271 were interested in whether other cartilage and/or bony phenotypes would arise late in
272 embryogenesis. Accordingly, to visualize any phenotypes that develop late in embryogenesis, we
273 stained P1 CD1 and C57BL/6 male and female skulls with Alcian blue and Alizarin red to label
274 cartilage and bone, respectively. Consistent with previous P21 and P28 findings[25], doming of the
275 cranial vault was observed in all P1 PLX5622 CD1 male and female pups, with overt changes to
276 calvarial bone size and density, including impairments to sagittal and coronal suture
277 development (Figures 5A–5D'). Moreover, skull length was found to significantly decrease in P1
278 PLX5622 CD1 male and female pups as compared to control (Figure 5E; p<0.0001). Similar, but
279 milder, doming of the cranial vault was observed in P1 PLX5622 C57BL/6 male and female
280 pups (Figures S5A–S5B', arrows). However, disruption to calvarial bone size and density,
281 including impairments to sagittal and interfrontal sutures (Figures S5C–S5D'), were still
282 prominent in P1 PLX5622 C57BL/6 male and female pups as compared to control. In contrast,
283 skull length was not significantly impacted by PLX5622 exposure (Figure S5E; p=0.6869).
284
285 When focusing on the Pl CD1 mandible (Figures 5F-G'), we began to observe notable sex
286 differences in mandible length (Figure 5H; significant effect of diet $F_{(1,20)}$=17.88, p=0.0004 and

287 diet x sex interaction $F_{(1,20)}$=4.717, p=0.0421) and height (Figure 5I; significant effect of diet
288 $F_{(1,20)}$=151.6, p<0.0001 and sex $F_{(1,20)}$=8.754, p=0.0078) in response to embryonic PLX5622
289 exposure. Indeed, only P1 PLX5622 CD1 female pups had shorter mandibles (Figure 5H; female
290 p=0.0011), while P1 CD1 control and PLX5622 male mandibles presented with comparable
291 lengths (Figure 5H; male p=0.4821). While P1 PLX5622 CD1 mandible height significantly
292 decreased in both sexes (Figure 5I; male p<0.0001, female p<0.0001), a greater disruption was
293 observed in P1 PLX5622 CD1 female pups (Figure 5I; PLX5622 diet male vs. female p=0.0313).
294 In contrast, P1 control and PLX5633 C57BL/6 male and female mandible length was comparable
295 (Figures S5F–S5H; p=0.6283), while mandible height was significantly decreased in both P1
296 PLX5622 C57BL/6 males and females alike (Figure S5I; p<0.0001).
297
298 In assessing the P1 CD1 ear, we observed notable abnormalities to the ear ossicles, including an
299 absence of the incus in PLX5622 male and female pups as compared to controls, and prominent
300 disruptions to the malleus and stapes (Figures 5J–5K'). Bone density was disrupted in the otic
301 capsule and tympanic ring (Figures 5J–5K'), which was also found to be significantly shorter in
302 PLX5622 CD1 males and females alike (Figure 5L; p<0.0001). Interestingly, we observed sex
303 differences with respect to tympanic ring thickness (Figure 5M; significant effect of diet
304 $F_{(1,20)}$=43.62, p<0.0001 and sex $F_{(1,20)}$=11.42, p=0.0030). While the P1 PLX5622 CD1 tympanic
305 ring was significantly thicker in both sexes (Figure 5M; male p<0.0001, female p=0.0090), a
306 larger disruption was observed in P1 PLX5622 CD1 male pups (Figure 5M; PLX5622 diet male
307 vs. female p=0.0120). Interestingly, the P1 control C57BL/6 ear appeared less developed than
308 what was observed at P1 in CD1 pups (compare Figures 5J-K' to Figures S5J–S5K'), as the
309 incus was absent. However, both the P1 C57BL/6 male and female malleus and stapes were

310 similarly underdeveloped after embryonic exposure to PLX5622 (Figures S5J-5K', arrows).
311 Similar to the incus, the otic capsule appeared underdeveloped in the P1 control C57BL/6 ear as
312 compared to what was observed in CD1 pups (compare Figures 5J-K' to Figures S5J–S5K'); yet
313 otic capsule mineralization was found to be disrupted in P1 PLX5622 C57BL/6 male and female
314 pups when compared to control (Figures S5J–S5K', triangles). Surprisingly, analysis of tympanic
315 ring length (Figures S5J–S5K', arrowheads) showed sex differences (Figure S5L; significant
316 effect of diet $F_{(1,20)}$=19.06, p=0.0003 and diet x sex interaction $F_{(1,20)}$=4.939, p=0.0380), whereby
317 P1 control C57BL/6 female tympanic ring length was found to be significantly different from P1
318 control C57BL/6 male pups (Figure S5L; p=0.0490), and PLX5622 exposure was only found to
319 impact tympanic ring length in P1 PLX5622 C57BL/6 male pups (Figure S5L; male p=0.0008,
320 female p=0.4474). In contrast, tympanic ring thickness was significantly increased in both P1
321 PLX5622 C57BL/6 males and females alike (Figure S5M; p<0.0001).
322
323 Intriguingly, P1 PLX5622 CD1 male and female pups also presented with disruptions to the
324 palate, palatine sutures, and premaxilla when compared to controls (Figures 5N-5O').
325 Abnormalities in P1 PLX5622 CD1 male and female pup cranial base development, including
326 smaller basisphenoid and palatine bones, wider spheno-occipital and intersphenoid
327 synchondroses, and morphological alterations to the palatine-basisphenoid sutures, could also be
328 observed (Figures 5P-5Q'). Disruptions to the palate, palatine processes, and premaxilla
329 appeared milder in Pl PLX5622 C57BL/6 male and female pups (Figures S5N–S5O'). Similarly,
330 subtle abnormalities were observed in the cranial base of Pl PLX5622 C57BL/6 male and female
331 pups, including a smaller basisphenoid bone and wider spheno-occipital and intersphenoid
332 synchondroses, while the palatine bones and palatine sutures did not appear to be impacted

333 (Figures S5P-S5Q'). Taken together, these data suggest that CSF1R+ cells play important and
334 widespread roles in craniofacial bone morphogenesis. Notably, we also observed sex differences,
335 with male-specific phenotypes in the ear and a female-specific phenotype in the mandible, in
336 addition to strain-dependent effects, with C57BL/6 pups presenting milder phenotypes overall.
337

338 **Skull Doming in PLX5622 Pups is Not Caused by Craniosynostosis**

339 As doming of the cranial vault is often associated with midface hypoplasia and a shortened
340 cranial base[39-44], the cranial base of P1 control and PLX5622 CD1 male and female pups were
341 also evaluated by micro-computed tomography (μCT; Figures S6A–S6D). No disruptions to
342 posterior cranial base length (Figure S6E; p=0.1447) or anterior frontal complex length (Figure
343 S6F; p=0.6624) were observed between P1 control and PLX5622 CD1 male and female pups.
344 Similarly, no significant differences were observed in the lengths of the basioccipital (Figure
345 S6G; p=0.0569) or basisphenoid (Figure S6H; p=0.3632) bones when comparing P1 control and
346 PLX5622 CD1 male and female pups; however, the presphenoid bone was significantly shorter
347 in P1 PLX5622 CD1 male and female pups (Figure S6I; p=0.0002). While the spheno-occipital
348 synchondrosis was comparable between P1 control and PLX5622 CD1 male and female pups
349 (Figure S6J; p=0.0713), P1 PLX5622 CD1 male and female pups presented with wider inter-
350 sphenoid synchondroses (Figure S6K; p=0.0005).
351

352 As hydrocephalus could also be contributing to skull doming[45-50], contrast enhanced μCT was
353 used to examine the gross morphology of P1 control and PLX5622 CD1 male and female pup
354 brains (Figures S6L–S6S). Ventriculomegaly of the lateral and third ventricles, in addition to
355 bilateral cavitary lesions at the cortico-striato-amygdalar boundary, could be observed both

356 rostrally (Figures S6L-O, arrows) and caudally (Figures S6P-S6S, arrows) when comparing P1
357 PLX5622 CD1 male and female pups to controls. Overall, while our data suggests that PLX5622
358 pups do not display craniosynostosis, exposure to PLX5622 during embryogenesis does drive
359 disruptions to the cranial base and structural changes to the gross morphology of the brain.
360

361 **Gestational Exposure to PLX5622 Alters Cytokine and Chemokine Secretion from CSF1R+**
362 **Cells**

363 Given that macrophages are known to secrete cytokines and chemokines, which are capable of
364 stimulating tissue growth postnatally[21,51] and during wound healing[52,53], we next investigated
365 whether PLX5622 exposure disrupts CSF1R+ cell-derived secreted factors to contribute to the
366 reported craniofacial phenotypes. Luminex analysis of cytokines and chemokines secreted from
367 cultured E13.5 control and PLX5622 male and female C57BL/6 craniofacial tissues (Figure 6A)
368 showed a significant downregulation of TNFα, G-CSF, IL-16, CCL2, CCL3, CCL4, CCL12,
369 CCL22, CXCL1, CXCL2, and CXCL10 (Figures 6B–6L; CXCL1 $p=0.0020$, all others
370 $p<0.0001$) upon PLX5622 exposure. Interestingly, we observed sex differences in IFNβ-1
371 (Figure 6M; main effect of diet $F_{(1,32)}=12.44$, $p=0.0013$), IL-6 (Figure 6N; main effect of diet
372 $F_{(1,32)}=21.86$, $p<0.0001$), CCL5 (Figure 6O; main effect of diet $F_{(1,32)}=15.73$, $p=0.0004$), and
373 CX3CL1 (Figure 6P; main effect of diet $F_{(1,32)}=26.64$, $p<0.0001$) levels. Specifically, IFNβ-1
374 (Figure 6M; male $p=0.3686$, female $p=0.0108$), IL-6 (Figure 6N; male $p=0.0561$, female
375 $p=0.0021$), and CCL5 (Figure 6O; male $p=0.3778$, female $p=0.0020$) were only found to be
376 significantly downregulated in E13.5 PLX5622 female craniofacial tissue cultures. In contrast,
377 CX3CL1 was only significantly upregulated in E13.5 PLX5622 male craniofacial tissue cultures
378 (Figure 6P; male $p=0.0003$, female $p=0.0532$). Although 33 other cytokines and chemokines

379 were assessed in our analyses, these secreted factors were either lowly expressed, not
380 significantly changed, or below the level of detection (Table S2).
381
382 To confirm that these cytokines and chemokines could indeed be derived from CSF1R+ cells in
383 craniofacial tissues, we analyzed publicly available single-cell RNA sequencing datasets from
384 E12.5 and E13.5 FVB/NJ and C57BL/6J craniofacial mesenchyme[54,55]. *Csf1r*-expressing cells
385 extracted from these datasets formed three distinct clusters, with clusters 1 and 2 upregulating
386 macrophage markers such as *Ptprc* and *Lyve1*, while cluster 3 expressed the osteoclast-specific
387 marker *Ctsk* (Figure S7A). Cluster 1 was found to express *Ccl2, Ccl3, Ccl4,* and *Ccl12*, while
388 cluster 2 only upregulated *Ccl12* (Figure S7A). Other cytokines and chemokines, such as *Cxcl2*,
389 *Cxcl10*, *IL16*, *Tnf*, etc., were not found to be upregulated in any of the clusters (Figure S7A).
390 Importantly, assessment of mRNA expression in the E15.5 mandible, maxilla, and ear (Figures
391 S7B–S7D) using fluorescent *in situ* hybridization revealed the presence of *Csf1r*/*Ccl4* double-
392 positive cells in each craniofacial tissue examined (Figures S7E-S7G). Moreover,
393 immunofluorescence staining of E15.5 craniofacial tissue cryosections also confirmed the
394 presence of CCL3 and CCL4 in *Csf1r*$^{EGFP+}$ cells in each of the craniofacial tissues assessed
395 (Figures S7H–S7S). Combined, these data suggest that embryonic exposure to PLX5622
396 significantly disrupts cytokine and chemokine levels in craniofacial tissues, with these changes
397 likely being primarily driven by CSF1R+ cells.
398
399 **CSF1R+ Cell Depletion Disrupts Neural Crest Proliferation**
400 To test whether the depletion of CSF1R+ cells and altered cytokine/chemokine signaling impact
401 surrounding cells to influence craniofacial morphogenesis, we focused on NCCs as many of the

402 craniofacial structures disrupted by PLX5622 exposure are derived from this lineage. To start, we
403 employed a neural crest-derived sphere assay to examine the impact of PLX5622 exposure on
404 NCCs (Figure 7A). Briefly, neural crest-derived cells were isolated from E12.5
405 *Wnt1*^{Cre};*Rosa26*^{tdTomato} control and PLX5622 male and female embryos and cultured in 24-well
406 plates for 10 days to allow for sphere formation[56]. Primary spheres were then dissociated and
407 cells were cultured for an additional 10 days to form secondary spheres. Primary and secondary
408 neural crest-derived spheres retained *Wnt1*^{Cre}-driven tdTomato+ signal and also expressed NCC
409 markers such as PDGFRα[57], SOX2[58,59], and SOX10[60,61], regardless of whether spheres were
410 derived from E12.5 control or PLX5622 embryos (Figures 7B–7M). Intriguingly, gestational
411 exposure to PLX5622 resulted in a significant decrease in the number of primary neural crest-
412 derived spheres (Figure 7N; p=0.0004), suggesting a reduced proliferative capacity of NCCs.
413
414 To validate that embryonic NCC proliferation was indeed decreased in response to gestational
415 PLX5622 exposure, we performed immunofluorescence staining on E15.5 *Wnt1*^{Cre};*Rosa26*^{tdTomato}
416 craniofacial tissue cryosections to quantify tdTomato+ cell numbers and proliferation using a
417 Ki67 antibody. *Wnt1*^{Cre}-driven tdTomato+ signal was found to be highly expressed within
418 mineralizing regions of craniofacial bones—particularly, in regions where we had previously
419 identified abnormal embryonic osteoblast staining/mineralization in response to PLX5622
420 exposure. Accordingly, we focused our analyses on the E15.5 premaxilla and mandible.
421 Quantification of *Wnt1*^{Cre}-driven tdTomato+ and Ki67+ cells (Figures 7O-S', arrows) in the
422 E15.5 male and female premaxilla showed a significant decrease in both tdTomato+ neural crest-
423 derived cells (Figure 7Q; p<0.0001) and Ki67+ proliferating cells (Figure 7T; p<0.0001) in
424 PLX5622 embryos as compared to control. Similarly, quantification of *Wnt1*^{Cre}-driven

425 tdTomato+ and Ki67+ cells (Figures 7U-Y', arrows) in the E15.5 male and female mandible
426 showed a significant decrease in tdTomato+ cells (Figure 7W; $p=0.0004$) and Ki67+ cells (Figure
427 7Z; $p<0.0001$) in PLX5622 embryos as compared to control. Taken together, these data suggest
428 that the proliferative capacity of cranial NCCs decreases in response to PLX5622 exposure.
429

430 **DISCUSSION**

431 This study is the first to provide an in-depth characterization of CSF1R+ macrophage and
432 osteoclast depletion in craniofacial tissues across embryogenesis in response to PLX5622
433 exposure[25-27,62-66]—a pharmacological tool that allows for temporal control and transient
434 depletion of CSF1R-expressing cells. Exposure to PLX5622 during gestation significantly
435 depleted CSF1R+ cells across embryogenesis, and either halts or significantly delays
436 osteoclastogenesis, leading to a loss of bone resorptive activity throughout the developing
437 craniofacial bones in the embryo. To our surprise, depleting CSF1R+ cells using PLX5622 does
438 not impact the gross morphology of craniofacial nerves or muscles in male or female CD1 or
439 C57BL/6 embryos. In contrast, craniofacial defects in the premaxilla and mandible appear as
440 early as E15.5, while abnormalities in skull shape, cranial sutures, ear ossicles, palate, and
441 cranial base development appear to arise later in embryogenesis, between E15.5 and birth.
442 Although our data suggest that craniosynostosis does not account for the skull doming in P1
443 PLX5622 pups, disruptions to the cranial base and/or structural changes to the gross morphology
444 of the brain could impact skull development and contribute to skull doming. Notably, we
445 observed sex differences in P1 PLX5622 pups, whereby males presented with more prominent
446 ear phenotypes and females displayed greater disruptions to the mandible. We also observed
447 strain-dependent effects, with overall stronger phenotypes being observed in CD1 pups than in

448 C57BL/6 pups. Interestingly, embryonic exposure to PLX5622 also significantly altered cytokine
449 and chemokine levels in craniofacial tissues, with these changes likely being primarily driven by
450 CSF1R+ cells—namely macrophages. These changes in signaling within craniofacial tissues
451 have the potential to alter CSF1R+ cell dynamics and interactions with neighbouring cells, which
452 could explain the observed decrease in proliferative capacity of NCCs in response to PLX5622
453 exposure. Altogether, a reduction in NCC proliferation in craniofacial tissues could contribute to
454 alterations in differentiation and osteogenic potential, resulting in the phenotypic disruptions in
455 the premaxilla and mandible, and likely the many other bony abnormalities seen in PLX5622
456 offspring.
457
458 In response to PLX5622 exposure from E3.5 onwards, CSF1R+ cell depletion was observed in
459 all tissues examined and remained relatively stable (~50%) across embryogenesis; however,
460 apoptotic cells accumulated predominantly in nervous and muscular structures and not in or
461 around developing cartilaginous/bony tissues, except for the ear. Indeed, programmed cell death
462 of mesenchyme at the retina-lens interface at E10 in C57BL/6J mice is essential for normal eye
463 development[67]; while, caspase-3 deficient C57BL/6 mice present with inner ear disruptions in
464 the cochlea and vestibule and severe auditory dysfunction, demonstrating that caspase-3-
465 dependent apoptosis is critical for normal inner ear development and function[68]. Moreover,
466 neuronal death has also been observed in normal trigeminal development in CD1 mice[69]. It is
467 interesting to note that eye defects were previously reported in some PLX5622-exposed mice,
468 where one eye could not be opened until later in adulthood[25]. Therefore, increased apoptosis
469 resulting from PLX5622 exposure could perturb normal apoptotic programs and disrupt
470 craniofacial morphogenesis, resulting in nerve and/or muscle phenotypes that could appear after

471 E15.5—especially since bone disruptions exist across nearly the entire PLX5622 head and
472 changes in the shape of mineralized tissue can directly impact craniofacial nerve and muscle
473 development[70-76]. For example, the shape of the temporalis muscle can change upon deformation
474 of the mandibular condyle, and the size of neurovascular bundles can be reduced upon removal
475 of teeth from the mandible[70,71]. Accordingly, craniofacial nerve and muscle development in
476 PLX5622-exposed offspring should be studied postnatally to confirm whether phenotypes in
477 these tissues eventually develop.
478
479 As *Csf1/Csf1r*-disrupted genetic models and the PLX5622 pharmacological depletion model both
480 display domed skulls[9-11,15,25,26,77-79], and skull doming can be caused by midface hypoplasia and
481 inhibited cranial base expansion[39-44], we thoroughly assessed the cranial base. Although cranial
482 base length was unaffected by PLX5622 exposure, suggesting that craniosynostosis and/or
483 cranial base hypoplasia is likely not responsible for the skull doming seen in PLX5622 pups, the
484 smaller cranial base bones and widened synchondroses observed in PLX5622 mice could
485 contribute to the skull phenotype. We also noted enlarged lateral and third ventricles in PLX5622
486 pups, suggesting that mild hydrocephalus could contribute to skull doming, which has been seen
487 in other animal models[45-50]. Moreover, we also observed brain lesions at the cortico-striato-
488 amygdalar boundary in PLX5622 pups—an area susceptible to physiological morphogenetic
489 stress that is essential for fetal brain morphogenesis[80]. Given that microglia play critical roles in
490 maintaining structural integrity at this boundary[80], the loss of microglia upon PLX5622 exposure
491 could disrupt normal maintenance and repair mechanisms, resulting in mechanical pressures on
492 the cranial vault and skull doming. However, it is also possible that insufficient mineralization
493 compromises the integrity of the calvaria such that it bulges outward in response to normal

494 mechanical forces of the developing brain. Interestingly, the morphological disruptions observed
495 in the brain and cranial base of PLX5622 mice are reminiscent of the brain abnormalities and
496 cranial base sclerosis observed in brain abnormalities, neurodegeneration, and dysosteosclerosis
497 (BANDDOS) patients—a human disorder caused by bi-allelic mutation in *CSF1R*[23,24,81-87]. The
498 skull doming, cranial suture impairments, and cranial base disruptions seen in PLX5622 mice
499 could be a useful model for studying the cranial vault malformations observed in
500 BANDDOS[23,24,81,83]; especially considering the titratable nature of PLX5622, as CSF1R
501 inhibition could more accurately reflect hypomorphic *CSF1R* mutations which account for 8/11
502 identified mutations causing BANDDOS[88].
503
504 Although the phenotypes seen in *Csf1r/CSF1R*-disrupted rodents and humans are of an
505 osteosclerotic nature[9,15,21,23,24,77,81,83,89,90], likely due to a lack of osteoclasts, we observed
506 decreased bone formation in the calvaria of PLX5622 pups and a reduction in the size of the
507 premaxilla, mandible, ear bones, palate, and cranial base. These phenotypes are unlikely to result
508 solely from a loss of bone resorption by osteoclasts. Instead, prenatal exposure to PLX5622
509 could disrupt signaling from CSF1R+ macrophages that are required for bone formation and
510 growth[21,91-96]. Intriguingly, these osteogenic pathways may also respond to PLX5622 differently
511 between sexes given the sex-specific mandible and ear phenotypes observed and sex-dependent
512 changes in several cytokines/chemokines. For example, IL-6 mediates bone loss due to estrogen
513 deficiency in ovariectomized female mice[97,98] and we observed a significant decrease in IL-6
514 uniquely in PLX5622 females, suggesting sex hormones may influence signaling to drive sex-
515 specific phenotypes. CSF1R+ osteoclasts are also more abundant and active in long bones of
516 female mice compared to males, resulting in decreased bone mass[99-101], and ovariectomy-induced

517 estrogen deficiency increases CSF1 production[102-104], which together further suggest a potential
518 for sex hormone-dependent responses to CSF1R+ cell depletion following PLX5622 exposure. It
519 is also interesting to note that we observed basal sex differences that were independent of
520 PLX5622 exposure, which are in line with sex differences observed in craniofacial bones that
521 can be observed at birth in humans[105], and highlight the importance of studying both sexes in
522 craniofacial research.
523
524 It is also valuable to study strain differences, as *Tcof1*$^{+/-}$ mice—a classic model of Treacher
525 Collins Syndrome—have phenotypes that are highly dependent on genetic background, with
526 CBA/Ca and C57BL/6 mice showing severe neural crest hypoplasia and craniofacial defects,
527 C3H/HEN mice displaying slightly milder impacts, and BALB/c and DBA/1 presenting near-
528 normal development[106]. To avoid embryonic lethality on the C57BL/6J background,
529 *Fgfr2c*$^{C342Y/+}$ Crouzon syndrome mice are maintained on a CD1 background[107]. These mice show
530 similarities to *Fgfr2*$^{+/S252W}$ Apert syndrome mice on the C57BL/6 background, exhibiting skull
531 and brain phenotypes due to craniosynostosis[107,108]. Other genetic deletion mutant models also
532 report increased penetrance of craniofacial defects in the C57BL/6 inbred background when
533 compared to mixed or CD1 outbred background[109-112]. In contrast, in the current study, CD1 mice
534 exhibited more severe craniofacial bone phenotypes than C57BL/6 mice in response to PLX5622
535 exposure. Perhaps genotypic differences result in divergent expression patterns of signaling
536 factors during craniofacial morphogenesis, for example, *Meox-2* and *Fgfr1* patterning differences
537 during palatal development between inbred C57BL/6 and outbred Swiss Webster and Black
538 Swiss strains[113]. Strain differences in timing of morphogenetic events could also interact with the
539 kinetics of CSF1R+ cell depletion to mediate the difference in craniofacial phenotypes. The use

540 of PLX5622 in further inbred/outbred mouse models and the analysis of signaling changes in
541 each strain could deepen our understanding of how genetic background impacts CSF1R-
542 expressing cells in craniofacial development.
543
544 Interestingly, the impact of PLX5622 exposure on osteogenesis appears to be independent of
545 whether the bone is formed by intramembranous (calvaria) or endochondral ossification
546 (auditory ossicles)[114-122]. This suggests that signaling alterations may act on a common
547 progenitor, which is supported by our findings as PLX5622 exposure alters cytokine/chemokine
548 levels and NCCs give rise to the majority of the craniofacial bones found to be disrupted in
549 PLX5622 mice[123-128]. Accordingly, decreases in NCC proliferation and total numbers in
550 PLX5622 embryos could be an underlying factor that contributes to the smaller bone sizes seen
551 in PLX5622 pups. As mentioned above, the *Tcof1*$^{+/-}$ mouse presents with multiple craniofacial
552 malformations that result from NCC deficiency[106,129-133]. Similar to PLX5622 mice, *Tcof1*$^{+/-}$ mice
553 exhibit hypoplasia of the calvaria, premaxilla, mandible, and otic capsule. However, *Tcof1*$^{+/-}$
554 mice also present with incomplete midline fusion, cleft palate, and lack of a nasal septum—
555 phenotypes driven by increased apoptosis and decreased proliferation of NCCs[106,129,131-133]. Since
556 PLX5622 exposure did not increase apoptosis in most tissues, especially in and around cartilage
557 and bones, a milder NCC deficiency due to reduced proliferation alone may explain why only a
558 subset of craniofacial phenotypes are shared between *Tcof1*$^{+/-}$ and PLX5622 mice. Although
559 craniofacial nerves arise from NCCs[134,135], they appear unimpacted by PLX5622 exposure during
560 embryogenesis, which could suggest that unique signals—such as those identified herein—
561 influence NCC differentiation differently depending on the surrounding environment and tissue.
562

563 Indeed, NCCs do respond to several of the cytokines/chemokines disrupted by PLX5622,
564 including CCL2 which induces NCC migration into the mouse heart[136], and CXCL1 and IL-6
565 which mediate NCC differentiation into osteoblasts during intramembranous ossification in a
566 mouse calvarial defect model[137]. CCL2 and CXCL1 are also chemoattractants for osteoclast
567 precursors and osteoclastogenesis[138-143]; while altering the secretion of any number of the other
568 cytokines/chemokines found to change in our study, including CCL3, CCL4, CCL5, CCL12,
569 CCL22, CXCL2, CXCL10, G-CSF, IFNβ-1 and/or TNFα, could impact osteoclast function and
570 bone remodeling[144-162]. Uniquely, IL-6 has been shown to be a critical regulator of bone
571 remodeling by negatively regulating osteoblasts and modulating osteoclast numbers and
572 resorption[97,163-166]. The downregulation of these signals in PLX5622-exposed mice could impact
573 recruitment and differentiation of osteoblast and osteoclast precursors and disrupt bone
574 remodeling processes necessary for normal craniofacial bone morphogenesis. Specifically, the
575 decreases in bone size could be caused by reduced NCC proliferation and subsequent NCC
576 deficiency, while the increased bone density observed from E15.5 onwards may be driven by
577 decreased bone resorption and remodeling[167-171]. Alternatively, increased osteogenesis could
578 reflect premature NCC differentiation into osteoblasts—possibly in response to altered CXCL1
579 and IL-6 signaling[137], resulting in NCC progenitor deficiencies[172-174]. Although it is unclear how
580 the disruptions to NCCs and osteoclast precursors/osteoclastogenesis culminate in the phenotypic
581 disruptions seen in PLX5622 offspring, our findings suggest that CSF1R+ macrophages are a
582 likely source for the many cytokines/chemokines found to be altered in response to PLX5622
583 exposure and may mediate NCC and/or osteoclast deficiencies.
584

585 Intriguingly, CSF1R+ macrophages have also been shown to directly touch and physically
586 interact with NCCs to impact their differentiation programs[175]. Indeed, P2RY12+ microglia-like
587 macrophages in the human embryo epidermis regulate NCC differentiation into melanocytes, as
588 PLX5622 exposure in *ex vivo* cultures can deplete these macrophages and reduce melanocytic
589 NCC differentiation[175]—a finding similar to the neural crest-derived melanophore defects seen in
590 macrophage-ablated zebrafish[176]. Macrophages have also been shown to be essential for
591 mediating NCC reduction in nonylphenol-exposed rat colon and in limiting excessive neural
592 crest-derived auditory glial cell numbers in CD11b$^{DTR/EGFP}$ mice[177,178]. Therefore, it is possible
593 that direct contact between craniofacial macrophages and NCCs could impact NCC proliferation
594 and/or differentiation programs to influence craniofacial morphogenesis and drive the phenotypic
595 disruptions observed in PLX5622 mice. Although there is a lack of understanding of how
596 macrophages regulate NCC development, especially in the context of craniofacial
597 morphogenesis, we show that CSF1R+ macrophage depletion results in decreased NCC
598 proliferation and widespread craniofacial bone defects.
599
600 By exploring the impact of CSF1R+ macrophage and osteoclast depletion on craniofacial
601 morphogenesis in the embryo, we demonstrated that CSF1R-expressing cells are required for
602 normal development of the skull, cranial sutures, premaxilla, mandible, ear ossicles, palate, and
603 cranial base. Additionally, we showed that embryonic exposure to the CSF1R inhibitor PLX5622
604 drives sex, strain, and time-dependent disruptions in craniofacial bone development. Taken
605 together, these data highlight an underappreciated role for CSF1R+ macrophages and osteoclasts
606 in craniofacial morphogenesis during the embryonic period and suggest that altered interactions
607 with and/or signaling to NCCs may underlie the phenotypes observed in PLX5622 offspring.

608 **RESOURCE AVAILABILITY**

609 **Lead contact**

610 Requests for further information and resources and reagents should be directed to and will be
611 fulfilled by the lead contact, Dr. Jessica M. Rosin (jessica.rosin@ubc.ca).

612 **Materials availability**

613 This study did not generate new unique reagents.

614 **Data and code availability**

615 • This paper analyzes existing, publicly available data, accessible at the NCBI GEO
616 database: GSM5324643, GSM6146223, and GSM7508877.
617 • All data reported in this paper will be shared by the lead contact upon request.
618 • This paper does not report original code.
619 • Seurat codes used for analysis of publicly available datasets deposited on GEO are
620 available upon request.
621 • Any additional information required to reanalyze the data reported in this paper is
622 available from the lead contact upon request.

623

624 **ACKNOWLEDGEMENTS**

625 The authors thank Andrew Johnson and Justin Wong from the UBC Flow Core Facility for help
626 with FACS, the UBC Centre for High-Throughput Phenogenomics—a facility supported by the
627 Canada Foundation for Innovation, British Columbia Knowledge Development Foundation, and
628 the UBC Faculty of Dentistry—for help with μCT scans, and the UBC Centre for Disease
629 Modeling for animal care. We would also like to acknowledge Shruti S. Tophkhane, Joaquin I.
630 Henriquez, Katherine Fu, Joy M. Richman and the entire Richman Lab for help with micromass

631 culture and TRAP staining, and Siddharth R. Vora for help with the μCT scans. F.M. was
632 supported by an NSERC PGS-D (579343-2023), a UBC Four Year Doctoral Fellowship, and a
633 UBC Faculty of Dentistry Joseph Tonzetich Fellowship. R.R.J.Z. was supported by a UBC
634 Faculty of Dentistry Summer Research Award (2022 & 2023) and a Charles Shuler Research
635 Fellow award (2023). I.Z. and S.O. were supported by a UBC Faculty of Dentistry Summer
636 Research Award (2025). V.B.W. was supported by an NSERC USRA. This work was supported
637 by an NSERC Discovery Grant to J.M.R. (RGPIN-2022-03718). J.M.R. is a Michael Smith
638 Health Research (MSHR) BC Scholar and a Tier 2 Canada Research Chair (CRC) in Immune
639 Regulation of Developmental Programs.
640

641 **AUTHOR CONTRIBUTIONS**

642 Conceptualization, F.M. and J.M.R.; data curation, F.M., M.R., and R.O.; formal analysis, F.M.,
643 R.O., and J.M.R.; funding acquisition, J.M.R.; investigation, F.M., R.R.J.Z., M.R., I.Z., S.O.,
644 R.O., V.B.W., and J.M.R.; methodology, F.M., M.R., R.O., and J.M.R.; project administration,
645 J.M.R.; resources, F.M., M.R., and J.M.R.; software, F.M. and R.O.; supervision, J.M.R.;
646 validation, F.M., M.R., R.O., and J.M.R.; visualization, F.M., M.R., R.O., and J.M.R.; writing—
647 original draft, F.M. and J.M.R.; writing—review & editing, F.M., M.R., and J.M.R.
648

649 **DECLARATION OF INTERESTS**

650 The authors declare no competing interests.
651

652 **SUPPLEMENTAL INFORMATION**

653 **Document S1. Figures S1–S7, Tables S1–S3, and supplemental references**

654 **FIGURE TITLES AND LEGENDS**

655 **Figure 1. Gestational Exposure to PLX5622 Significantly Depletes CSF1R-Expressing**
656 **Cells.** (A) Schematic illustrating collection of *Csf1r*$^{EGFP+}$ cells from craniofacial tissues for flow
657 cytometry. (B) Quantification of EGFP+ cells from *Csf1r*^{EGFP} craniofacial tissues using flow
658 cytometry (N=9-15 embryos per treatment/time-point from 2-4 dams). (C-W)
659 Immunofluorescent images and quantification of CSF1R+ and *Csf1r*$^{EGFP+}$ cells in and around the
660 E15.5 nasal septum (n.s.; C-E), Meckel's cartilage (m.c.; F-H), ear (I-K), maxillary incisor (L-
661 N), eye (ey; O-Q), trigeminal (R-T), and tongue (tg; U-W). Arrows mark CSF1R and *Csf1r*^{EGFP}
662 double-positive cells in control and PLX5622 embryos (N=3 embryos per sex/treatment from 2-3
663 dams). Abbreviations: c.d., cochlear duct; d.p., dental papilla; e.k., enamel knot; l.s.c., lateral
664 semicircular canal; s.r., stellate reticulum; ut, utricle. Blue dots represent male and pink dots
665 represent female. Counts represent mean ± SEM and were analyzed by a two-tailed unpaired t-
666 test.

667

668 **Figure 2. Prenatal Exposure to PLX5622 Disrupts Osteoclast Development and Function.**
669 (A-D') Multinucleated *Csf1r*$^{EGFP+}$ osteoclasts (arrows) in the E15.5 premaxilla (A-B') and
670 maxilla (C-D'). (E-I) Immunofluorescent images (E-H) and quantification (I) of multinucleated
671 CTSK/*Csf1r*^{EGFP} double-positive osteoclasts (arrows, left graph) and *Csf1r*$^{EGFP+}$ single-positive
672 osteoclasts (right graph) in the E15.5 control and PLX5622 mandible. (J-S') TRAP staining
673 (arrows) in E15.5 control and PLX5622 mandible (md; J-K'), maxilla (mx; L-M'), frontal (fr; N-
674 O'), basioccipital (bo; P-Q'), and exoccipital (eo; R-S') bones. N=3 embryos per sex/treatment
675 from 2-3 dams. Abbreviations: m.c, Meckel's cartilage; pmx, premaxilla. Blue dots represent

676 male and pink dots represent female. Counts represent mean ± SEM and were analyzed by a two-
677 tailed unpaired t-test.
678
679 **Figure 3. Exposure to PLX5622 During Embryogenesis Increases Bone Density in the**
680 **Premaxilla and Mandible.** (A-J') E15.5 Sp7 osteoblast staining in the premaxilla (pmx; A-B')
681 mandible (md; C-D'), maxilla (mx; E-F'), frontal (fr; G-H'), and basioccipital (bo; I-J') bones of
682 control and PLX5622 CD1 embryos. (K-T') E15.5 von Kossa and Alcian blue staining in the
683 premaxilla (K-L'), mandible (M-N') maxilla (O-P'), frontal (Q-R'), and basioccipital (S-T')
684 bones of control and PLX5622 CD1 embryos. Arrows highlight changes in bone density (A-D',
685 K-N'). N=3 embryos per sex/treatment from 2-3 dams. Abbreviations: m.c, Meckel's cartilage.
686
687 **Figure 4. Gestational Exposure to PLX5622 Increases Osteogenesis in Embryonic Facial**
688 **Micromass Cultures.** (A and G) Schematic illustrating micro-dissected area for collecting
689 mesenchymal cells from the E12.5 CD1 frontonasal mass (A) and mandible (G) for micromass
690 culture. (B-F, H-L) Alkaline phosphatase (Alk. phos. or ALP), Alcian blue, and hematoxylin
691 staining and quantification of E12.5 micromass cultures collected from the frontonasal mass (B-
692 F) and mandible (H-L) of control and PLX5622 embryos. N=12-14 cultures per treatment from 3
693 dams. Blue dots represent male, pink dots represent female, and black dots represent pooled
694 cultures with mixed sexes. Counts represent mean ± SEM and were analyzed by a two-tailed
695 unpaired t-test.

696

697 **Figure 5. Prenatal Exposure to PLX5622 Disrupts Craniofacial Bone Morphogenesis.**
698 (A-B') Lateral view of P1 CD1 cranial vault (arrows) in control and PLX5622 pups. (C-D')
699 Dorsal view of P1 CD1 skulls highlights sagittal (arrows) and coronal (arrowheads) sutures in
700 control and PLX5622 pups. (E) Quantification of skull length in P1 control and PLX5622 CD1
701 pups. (F-I) Lateral view of P1 CD1 mandibles (F-G') and quantification of mandible length (H;
702 horizontal arrows) and height (I; vertical arrows) in control and PLX5622 pups. (J-M) Lateral
703 view of the P1 CD1 ear (J-K') and quantification of tympanic ring (t.r.) length (L) and thickness
704 (M) in control and PLX5622 pups. Arrows mark disrupted ossicle development of the incus (in;
705 absent in PLX5622 pups, asterisks), malleus (ma), and stapes (st). Triangles mark the otic
706 capsule and arrowheads mark the tympanic ring. (N-O') Ventral views of the P1 CD1 palate
707 highlight the hard palate (arrowheads), premaxilla (pmx; double-headed arrows), and palatine
708 sutures (arrows) in controls and PLX5622 pups. (P-Q') Ventral view of the P1 CD1 cranial base
709 shows (arrows) the basisphenoid (bs) and palatine bone (p.b.), the spheno-occipital and
710 intersphenoid synchondroses (asterisks), and palatine-basisphenoid sutures (arrowheads) in
711 control and PLX5622 pups. N=6 pups per sex/treatment from 3-4 dams. Abbreviations: bo,
712 basioccipital; fr, frontal bone; ip, interparietal bone; mx, maxilla; na, nasal bone; oc, occipital
713 bone; pa, parietal bone; p.p.mx., palatine process of the maxilla; p.p.p., palatine process of the
714 palatine; pt, pterygoid process. Blue dots represent male and pink dots represent female.
715 Measurements represent mean ± SEM and were analyzed by a two-tailed unpaired t-test or a
716 two-way ANOVA with Tukey's post hoc test.

717

718 **Figure 6. Exposure to PLX5622 During Embryogenesis Disrupts Cytokine and Chemokine**
719 **Secretion in Craniofacial Tissue Cultures.** (A) Schematic illustrating E13.5 C57BL/6
720 craniofacial tissue culture and Luminex multiplex analysis of secreted cytokines and chemokines
721 in culture media. (B-P) Cytokine/chemokine analysis of E13.5 craniofacial tissue culture media
722 collected from control and PLX5622 embryos that were significantly downregulated in both
723 sexes (B-L); while IFNβ-1 (M), IL-6 (N), CCL5 (O), and CX3CL1 (P) were only statistically
724 significant in one sex. N=9 per sex/treatment from 3 dams. Blue dots represent male and pink
725 dots represent female. Quantifications represent mean ± SEM and were analyzed by a two-tailed
726 unpaired t-test or a two-way ANOVA with Tukey's post hoc test.

727

728 **Figure 7. Gestational Exposure to PLX5622 Decreases Neural Crest Proliferation.** (A)
729 Schematic illustrating the neural crest-derived sphere assay. (B-M) E12.5 *Wnt1*^{Cre}*; Rosa26*^{tdTomato}
730 control (B-G) and PLX5622 (H-M) primary (B, D, F, H, J, L) and secondary (C, E, G, I, K, M)
731 neural crest-derived spheres retain tdTomato+ signal and express PDGFRα (B, C, H, I), SOX2
732 (D, E, J, K), and SOX10 (F, G, L, M). (N) Primary sphere quantification of neural crest-derived
733 spheres from control and PLX5622 embryos (N=9-14 embryos per treatment from 2-3 dams).
734 (O-Z) Immunofluorescent images of E15.5 *Wnt1*^{Cre}-driven tdTomato+ signal (O-P', U-V') and
735 Ki67 staining (R-S', X-Y') in the premaxilla (pmx; O-T) and mandible (U-Z). (Q, T, W, Z)
736 Quantification of tdTomato+ (Q, W) and Ki67+ (T, Z) cells in control and PLX5622 embryos.
737 White lines mark the tissue regions used for quantifications (N=3 embryos per sex/treatment
738 from 3 dams). Abbreviations: DIV, days *in vitro*; m.c., Meckel's cartilage. Blue dots represent

739 male and pink dots represent female. Counts represent mean ± SEM and were analyzed by a two-
740 tailed unpaired t-test.
741
742
743
744
745
746
747
748
749
750
751
752
753
754
755
756
757
758
759
760
761

REFERENCES

1. Arai, F., Miyamoto, T., Ohneda, O., Inada, T., Sudo, T., Brasel, K., Miyata, T., Anderson, D.M., and Suda, T. (1999). Commitment and Differentiation of Osteoclast Precursor Cells by the Sequential Expression of C-Fms and Receptor Activator of Nuclear Factor κb (Rank) Receptors. Journal of Experimental Medicine *190*, 1741-1754. 10.1084/jem.190.12.1741.
2. Boulakirba, S., Pfeifer, A., Mhaidly, R., Obba, S., Goulard, M., Schmitt, T., Chaintreuil, P., Calleja, A., Furstoss, N., Orange, F., et al. (2018). IL-34 and CSF-1 display an equivalent macrophage differentiation ability but a different polarization potential. Sci Rep *8*, 256. 10.1038/s41598-017-18433-4.
3. Marks, D.C., Csar, X.F., Wilson, N.J., Novak, U., Ward, A.C., Kanagasundarum, V., Hoffmann, B.W., and Hamilton, J.A. (1999). Expression of a Y559F Mutant CSF-1 Receptor in M1 Myeloid Cells: A Role for Src Kinases in CSF-1 Receptor-Mediated Differentiation. Molecular Cell Biology Research Communications *1*, 144-152. https://doi.org/10.1006/mcbr.1999.0123.
4. Giulian, D., and Ingeman, J.E. (1988). Colony-stimulating factors as promoters of ameboid microglia. J Neurosci *8*, 4707-4717. 10.1523/JNEUROSCI.08-12-04707.1988.
5. Tushinski, R.J., Oliver, I.T., Guilbert, L.J., Tynan, P.W., Warner, J.R., and Stanley, E.R. (1982). Survival of mononuclear phagocytes depends on a lineage-specific growth factor that the differentiated cells selectively destroy. Cell *28*, 71-81. 10.1016/0092-8674(82)90376-2.
6. Feng, X., Takeshita, S., Namba, N., Wei, S., Teitelbaum, S.L., and Ross, F.P. (2002). Tyrosines 559 and 807 in the cytoplasmic tail of the macrophage colony-stimulating factor receptor play distinct roles in osteoclast differentiation and function. Endocrinology *143*, 4868-4874. 10.1210/en.2002-220467.
7. Chihara, T., Suzu, S., Hassan, R., Chutiwitoonchai, N., Hiyoshi, M., Motoyoshi, K., Kimura, F., and Okada, S. (2010). IL-34 and M-CSF share the receptor Fms but are not identical in biological activity and signal activation. Cell Death Differ *17*, 1917-1927. 10.1038/cdd.2010.60.
8. Delaney, C., Farrell, M., Doherty, C.P., Brennan, K., O'Keeffe, E., Greene, C., Byrne, K., Kelly, E., Birmingham, N., Hickey, P., et al. (2021). Attenuated CSF-1R signalling drives cerebrovascular pathology. EMBO Mol Med *13*, e12889. 10.15252/emmm.202012889.
9. Dai, X.M., Ryan, G.R., Hapel, A.J., Dominguez, M.G., Russell, R.G., Kapp, S., Sylvestre, V., and Stanley, E.R. (2002). Targeted disruption of the mouse colony-stimulating factor 1 receptor gene results in osteopetrosis, mononuclear phagocyte deficiency, increased primitive progenitor cell frequencies, and reproductive defects. Blood *99*, 111-120. 10.1182/blood.v99.1.111.
10. Marks, S.C., Jr., and Lane, P.W. (1976). Osteopetrosis, a new recessive skeletal mutation on chromosome 12 of the mouse. J Hered *67*, 11-18. 10.1093/oxfordjournals.jhered.a108657.
11. Pridans, C., Raper, A., Davis, G.M., Alves, J., Sauter, K.A., Lefevre, L., Regan, T., Meek, S., Sutherland, L., Thomson, A.J., et al. (2018). Pleiotropic Impacts of Macrophage and Microglial Deficiency on Development in Rats with Targeted Mutation of the Csf1r Locus. J Immunol *201*, 2683-2699. 10.4049/jimmunol.1701783.
12. Van Wesenbeeck, L., Odgren, P.R., MacKay, C.A., D'Angelo, M., Safadi, F.F., Popoff, S.N., Van Hul, W., and Marks, S.C., Jr. (2002). The osteopetrotic mutation toothless (tl) is

a loss-of-function frameshift mutation in the rat Csf1 gene: Evidence of a crucial role for CSF-1 in osteoclastogenesis and endochondral ossification. Proc Natl Acad Sci U S A *99*, 14303-14308. 10.1073/pnas.202332999.

13. Pollard, J.W., Hunt, J.S., Wiktor-Jedrzejczak, W., and Stanley, E.R. (1991). A pregnancy defect in the osteopetrotic (opop) mouse demonstrates the requirement for CSF-1 in female fertility. Developmental Biology *148*, 273-283. https://doi.org/10.1016/0012-1606(91)90336-2.
14. Erblich, B., Zhu, L., Etgen, A.M., Dobrenis, K., and Pollard, J.W. (2011). Absence of colony stimulation factor-1 receptor results in loss of microglia, disrupted brain development and olfactory deficits. PLoS One *6*, e26317. 10.1371/journal.pone.0026317.
15. Okano, T., and Kishimoto, I. (2019). Csf1 Signaling Regulates Maintenance of Resident Macrophages and Bone Formation in the Mouse Cochlea. Frontiers in Neurology *10*. 10.3389/fneur.2019.01244.
16. Sundquist, K., Cecchini, M., and Marks Jr, S. (1995). Colony-stimulating factor-1 injections improve but do not cure skeletal sclerosis in osteopetrotic (op) mice. Bone *16*, 39-46.
17. Begg, S.K., Radley, J.M., Pollard, J.W., Chisholm, O.T., Stanley, E.R., and Bertoncello, I. (1993). Delayed hematopoietic development in osteopetrotic (op/op) mice. Journal of Experimental Medicine *177*, 237-242. 10.1084/jem.177.1.237.
18. Cecchini, M.G., Dominguez, M.G., Mocci, S., Wetterwald, A., Felix, R., Fleisch, H., Chisholm, O., Hofstetter, W., Pollard, J.W., and Stanley, E.R. (1994). Role of colony stimulating factor-1 in the establishment and regulation of tissue macrophages during postnatal development of the mouse. Development *120*, 1357-1372. 10.1242/dev.120.6.1357.
19. Wiktor-Jedrzejczak, W.W., Ahmed, A., Szczylik, C., and Skelly, R.R. (1982). Hematological characterization of congenital osteopetrosis in op/op mouse. Possible mechanism for abnormal macrophage differentiation. J Exp Med *156*, 1516-1527. 10.1084/jem.156.5.1516.
20. Hume, D.A., Caruso, M., Ferrari-Cestari, M., Summers, K.M., Pridans, C., and Irvine, K.M. (2020). Phenotypic impacts of CSF1R deficiencies in humans and model organisms. Journal of Leukocyte Biology *107*, 205-219. https://doi.org/10.1002/JLB.MR0519-143R.
21. Keshvari, S., Caruso, M., Teakle, N., Batoon, L., Sehgal, A., Patkar, O.L., Ferrari-Cestari, M., Snell, C.E., Chen, C., Stevenson, A., et al. (2021). CSF1R-dependent macrophages control postnatal somatic growth and organ maturation. PLoS Genet *17*, e1009605. 10.1371/journal.pgen.1009605.
22. Patkar, O.L., Caruso, M., Teakle, N., Keshvari, S., Bush, S.J., Pridans, C., Belmer, A., Summers, K.M., Irvine, K.M., and Hume, D.A. (2021). Analysis of homozygous and heterozygous Csf1r knockout in the rat as a model for understanding microglial function in brain development and the impacts of human CSF1R mutations. Neurobiol Dis *151*, 105268. 10.1016/j.nbd.2021.105268.
23. Guo, L., Bertola, D.R., Takanohashi, A., Saito, A., Segawa, Y., Yokota, T., Ishibashi, S., Nishida, Y., Yamamoto, G.L., Franco, J., et al. (2019). Bi-allelic CSF1R Mutations Cause Skeletal Dysplasia of Dysosteosclerosis-Pyle Disease Spectrum and Degenerative Encephalopathy with Brain Malformation. Am J Hum Genet *104*, 925-935. 10.1016/j.ajhg.2019.03.004.

24. Monies, D., Maddirevula, S., Kurdi, W., Alanazy, M.H., Alkhalidi, H., Al-Owain, M., Sulaiman, R.A., Faqeih, E., Goljan, E., Ibrahim, N., et al. (2017). Autozygosity reveals recessive mutations and novel mechanisms in dominant genes: implications in variant interpretation. Genet Med *19*, 1144-1150. 10.1038/gim.2017.22.
25. Rosin, J.M., Vora, S.R., and Kurrasch, D.M. (2018). Depletion of embryonic microglia using the CSF1R inhibitor PLX5622 has adverse sex-specific effects on mice, including accelerated weight gain, hyperactivity and anxiolytic-like behaviour. Brain Behav Immun *73*, 682-697. 10.1016/j.bbi.2018.07.023.
26. Nagra, A., Katsube, M., Gao, W., Rosin, J.M., and Vora, S.R. (2023). Embryonic inhibition of colony-stimulating factor 1 receptor impacts craniofacial morphogenesis. Orthod Craniofac Res *26 Suppl 1*, 20-28. 10.1111/ocr.12671.
27. Yongzhen, L., Yan, G., Jing, L., Chenyan, R., Chuanqing, M., Yun, S., and Weihui, C. (2024). Embryonic inhibition of colony-stimulating factor 1 receptor induces enlarged cartilaginous zone of the midpalatal suture in postnatal mice. Orthod Craniofac Res *27*, 276-286. 10.1111/ocr.12724.
28. Care, A.S., Diener, K.R., Jasper, M.J., Brown, H.M., Ingman, W.V., and Robertson, S.A. (2013). Macrophages regulate corpus luteum development during embryo implantation in mice. J Clin Invest *123*, 3472-3487. 10.1172/JCI60561.
29. Wang, J., Xie, D., Liu, M., Gong, Y., Shi, X., Wei, J.Y., and Quan, S. (2016). Uterine macrophages affect embryo implantation via regulating vascular endothelial growth factor A in mice. Nan fang yi ke da xue xue bao = Journal of Southern Medical University *36*, 909-914.
30. Metschnikoff, E. (1891). Lecture on Phagocytosis and Immunity. Br Med J *1*, 213-217. 10.1136/bmj.1.1570.213.
31. van Furth, R., Cohn, Z.A., Hirsch, J.G., Humphrey, J.H., Spector, W.G., and Langevoort, H.L. (1972). The mononuclear phagocyte system: a new classification of macrophages, monocytes, and their precursor cells. Bull World Health Organ *46*, 845-852.
32. Bourez, R.L.J.H., Mathijssen, I.M.J., Vaandrager, J.M., and Vermeij-Keers, C. (1997). Apoptotic Cell Death During Normal Embryogenesis of the Coronal Suture: Early Detection of Apoptosis in Mice Using Annexin V. Journal of Craniofacial Surgery *8*, 441-445.
33. Dupe, V., Ghyselinck, N.B., Thomazy, V., Nagy, L., Davies, P.J., Chambon, P., and Mark, M. (1999). Essential roles of retinoic acid signaling in interdigital apoptosis and control of BMP-7 expression in mouse autopods. Dev Biol *208*, 30-43. 10.1006/dbio.1998.9176.
34. Tang, L.S., Santillano, D.R., Wlodarczyk, B.J., Miranda, R.C., and Finnell, R.H. (2005). Role of Folbp1 in the regional regulation of apoptosis and cell proliferation in the developing neural tube and craniofacies. Am J Med Genet C Semin Med Genet *135C*, 48-58. 10.1002/ajmg.c.30053.
35. Zakeri, Z., Quaglino, D., and Ahuja, H.S. (1994). Apoptotic cell death in the mouse limb and its suppression in the hammertoe mutant. Dev Biol *165*, 294-297. 10.1006/dbio.1994.1255.
36. Iyyanar, P.P.R., Qin, C., Adhikari, N., Liu, H., Hu, Y.C., Jiang, R., and Lan, Y. (2023). Developmental origin of the mammalian premaxilla. Dev Biol *503*, 1-9. 10.1016/j.ydbio.2023.07.005.

37. Richman, J.M., and Tickle, C. (1989). Epithelia are interchangeable between facial primordia of chick embryos and morphogenesis is controlled by the mesenchyme. Dev Biol *136*, 201-210. 10.1016/0012-1606(89)90142-5.
38. Wedden, S.E. (1987). Epithelial-mesenchymal interactions in the development of chick facial primordia and the target of retinoid action. Development *99*, 341-351. 10.1242/dev.99.3.341.
39. Vora, S.R. (2017). Mouse models for the study of cranial base growth and anomalies. Orthod Craniofac Res *20 Suppl 1*, 18-25. 10.1111/ocr.12180.
40. Eswarakumar, V.P., Horowitz, M.C., Locklin, R., Morriss-Kay, G.M., and Lonai, P. (2004). A gain-of-function mutation of Fgfr2c demonstrates the roles of this receptor variant in osteogenesis. Proc Natl Acad Sci U S A *101*, 12555-12560. 10.1073/pnas.0405031101.
41. Kawasaki, M., Izu, Y., Hayata, T., Ideno, H., Nifuji, A., Sheffield, V.C., Ezura, Y., and Noda, M. (2017). Bardet-Biedl syndrome 3 regulates the development of cranial base midline structures. Bone *101*, 179-190. 10.1016/j.bone.2016.02.017.
42. Laurita, J., Koyama, E., Chin, B., Taylor, J.A., Lakin, G.E., Hankenson, K.D., Bartlett, S.P., and Nah, H.D. (2011). The Muenke syndrome mutation (FgfR3P244R) causes cranial base shortening associated with growth plate dysfunction and premature perichondrial ossification in murine basicranial synchondroses. Dev Dyn *240*, 2584-2596. 10.1002/dvdy.22752.
43. Nagata, M., Nuckolls, G.H., Wang, X., Shum, L., Seki, Y., Kawase, T., Takahashi, K., Nonaka, K., Takahashi, I., Noman, A.A., et al. (2011). The primary site of the acrocephalic feature in Apert Syndrome is a dwarf cranial base with accelerated chondrocytic differentiation due to aberrant activation of the FGFR2 signaling. Bone *48*, 847-856. 10.1016/j.bone.2010.11.014.
44. Panda, S.P., Guntur, A.R., Polusani, S.R., Fajardo, R.J., Gakunga, P.T., Roman, L.J., and Masters, B.S. (2013). Conditional deletion of cytochrome p450 reductase in osteoprogenitor cells affects long bone and skull development in mice recapitulating antley-bixler syndrome: role of a redox enzyme in development. PLoS One *8*, e75638. 10.1371/journal.pone.0075638.
45. Schmidt, M., and Ondreka, N. Hydrocephalus in Animals.
46. Cohen, A.R., Leifer, D.W., Zechel, M., Flaningan, D.P., Lewin, J.S., and Lust, W.D. (1999). Characterization of a model of hydrocephalus in transgenic mice. J Neurosurg *91*, 978-988. 10.3171/jns.1999.91.6.0978.
47. Kohn, D.F., Chinookoswong, N., and Chou, S.M. (1981). A new model of congenital hydrocephalus in the rat. Acta Neuropathol *54*, 211-218. 10.1007/BF00687744.
48. Stottmann, R.W., Moran, J.L., Turbe-Doan, A., Driver, E., Kelley, M., and Beier, D.R. (2011). Focusing forward genetics: a tripartite ENU screen for neurodevelopmental mutations in the mouse. Genetics *188*, 615-624. 10.1534/genetics.111.126862.
49. Jimenez, A.J., Tome, M., Paez, P., Wagner, C., Rodriguez, S., Fernandez-Llebrez, P., Rodriguez, E.M., and Perez-Figares, J.M. (2001). A programmed ependymal denudation precedes congenital hydrocephalus in the hyh mutant mouse. J Neuropathol Exp Neurol *60*, 1105-1119. 10.1093/jnen/60.11.1105.
50. Yang, J., Simonneau, C., Kilker, R., Oakley, L., Byrne, M.D., Nichtova, Z., Stefanescu, I., Pardeep-Kumar, F., Tripathi, S., Londin, E., et al. (2019). Murine MPDZ-linked

943 hydrocephalus is caused by hyperpermeability of the choroid plexus. EMBO Mol Med
944 *11*. 10.15252/emmm.201809540.
945 51. Gow, D.J., Sester, D.P., and Hume, D.A. (2010). CSF-1, IGF-1, and the control of
946 postnatal growth and development. J Leukoc Biol *88*, 475-481. 10.1189/jlb.0310158.
947 52. Ploeger, D.T., Hosper, N.A., Schipper, M., Koerts, J.A., de Rond, S., and Bank, R.A.
948 (2013). Cell plasticity in wound healing: paracrine factors of M1/ M2 polarized
949 macrophages influence the phenotypical state of dermal fibroblasts. Cell Commun Signal
950 *11*, 29. 10.1186/1478-811X-11-29.
951 53. Weber, K.S., Nelson, P.J., Grone, H.J., and Weber, C. (1999). Expression of CCR2 by
952 endothelial cells : implications for MCP-1 mediated wound injury repair and In vivo
953 inflammatory activation of endothelium. Arterioscler Thromb Vasc Biol *19*, 2085-2093.
954 10.1161/01.atv.19.9.2085.
955 54. Angelozzi, M., Pellegrino da Silva, R., Gonzalez, M.V., and Lefebvre, V. (2022). Single-
956 cell atlas of craniogenesis uncovers SOXC-dependent, highly proliferative, and
957 myofibroblast-like osteodermal progenitors. Cell Rep *40*, 111045.
958 10.1016/j.celrep.2022.111045.
959 55. Rajderkar, S.S., Paraiso, K., Amaral, M.L., Kosicki, M., Cook, L.E., Darbellay, F.,
960 Spurrell, C.H., Osterwalder, M., Zhu, Y., Wu, H., et al. (2024). Dynamic enhancer
961 landscapes in human craniofacial development. Nat Commun *15*, 2030. 10.1038/s41467-
962 024-46396-4.
963 56. Lewis, A.E., Vasudevan, H.N., O'Neill, A.K., Soriano, P., and Bush, J.O. (2013). The
964 widely used Wnt1-Cre transgene causes developmental phenotypes by ectopic activation
965 of Wnt signaling. Dev Biol *379*, 229-234. 10.1016/j.ydbio.2013.04.026.
966 57. Schatteman, G.C., Morrison-Graham, K., van Koppen, A., Weston, J.A., and Bowen-
967 Pope, D.F. (1992). Regulation and role of PDGF receptor alpha-subunit expression during
968 embryogenesis. Development *115*, 123-131. 10.1242/dev.115.1.123.
969 58. Cai, J., Wu, Y., Mirua, T., Pierce, J.L., Lucero, M.T., Albertine, K.H., Spangrude, G.J.,
970 and Rao, M.S. (2002). Properties of a fetal multipotent neural stem cell (NEP cell). Dev
971 Biol *251*, 221-240. 10.1006/dbio.2002.0828.
972 59. Roellig, D., Tan-Cabugao, J., Esaian, S., and Bronner, M.E. (2017). Dynamic
973 transcriptional signature and cell fate analysis reveals plasticity of individual neural plate
974 border cells. Elife *6*. 10.7554/eLife.21620.
975 60. Kim, J., Lo, L., Dormand, E., and Anderson, D.J. (2003). SOX10 maintains multipotency
976 and inhibits neuronal differentiation of neural crest stem cells. Neuron *38*, 17-31.
977 10.1016/s0896-6273(03)00163-6.
978 61. Southard-Smith, E.M., Kos, L., and Pavan, W.J. (1998). Sox10 mutation disrupts neural
979 crest development in Dom Hirschsprung mouse model. Nat Genet *18*, 60-64.
980 10.1038/ng0198-60.
981 62. Bosch, A.J.T., Keller, L., Steiger, L., Rohm, T.V., Wiedemann, S.J., Low, A.J.Y., Stawiski,
982 M., Rachid, L., Roux, J., Konrad, D., et al. (2023). CSF1R inhibition with PLX5622
983 affects multiple immune cell compartments and induces tissue-specific metabolic effects
984 in lean mice. Diabetologia *66*, 2292-2306. 10.1007/s00125-023-06007-1.
985 63. Elmore, M.R.P., Hohsfield, L.A., Kramar, E.A., Soreq, L., Lee, R.J., Pham, S.T., Najafi,
986 A.R., Spangenberg, E.E., Wood, M.A., West, B.L., and Green, K.N. (2018). Replacement
987 of microglia in the aged brain reverses cognitive, synaptic, and neuronal deficits in mice.
988 Aging Cell *17*, e12832. 10.1111/acel.12832.

64. Hennen, E.M., Uppuganti, S., de la Visitacion, N., Chen, W., Krishnan, J., Vecchi Iii, L.A., Patrick, D.M., Siedlinski, M., Lemoli, M., Delgado, R., et al. (2025). Hypertension promotes bone loss and fragility by favoring bone resorption in mouse models. J Clin Invest. 10.1172/JCI184325.
65. Lei, F., Cui, N., Zhou, C., Chodosh, J., Vavvas, D.G., and Paschalis, E.I. (2020). CSF1R inhibition by a small-molecule inhibitor is not microglia specific; affecting hematopoiesis and the function of macrophages. Proc Natl Acad Sci U S A *117*, 23336-23338. 10.1073/pnas.1922788117.
66. Spangenberg, E., Severson, P.L., Hohsfield, L.A., Crapser, J., Zhang, J., Burton, E.A., Zhang, Y., Spevak, W., Lin, J., Phan, N.Y., et al. (2019). Sustained microglial depletion with CSF1R inhibitor impairs parenchymal plaque development in an Alzheimer's disease model. Nat Commun *10*, 3758. 10.1038/s41467-019-11674-z.
67. Silver, J., and Hughes, A.F. (1974). The relationship between morphogenetic cell death and the development of congenital anophthalmia. J Comp Neurol *157*, 281-301. 10.1002/cne.901570303.
68. Makishima, T., Hochman, L., Armstrong, P., Rosenberger, E., Ridley, R., Woo, M., Perachio, A., and Wood, S. (2011). Inner ear dysfunction in caspase-3 deficient mice. BMC Neurosci *12*, 102. 10.1186/1471-2202-12-102.
69. Davies, A., and Lumsden, A. (1984). Relation of target encounter and neuronal death to nerve growth factor responsiveness in the developing mouse trigeminal ganglion. J Comp Neurol *223*, 124-137. 10.1002/cne.902230110.
70. Wadu, S.G., Penhall, B., and Townsend, G.C. (1997). Morphological variability of the human inferior alveolar nerve. Clinical Anatomy *10*, 82-87. 10.1002/(sici)1098-2353(1997)10:2<82::Aid-ca2>3.0.Co;2-v.
71. Yamamoto, M., Takada, H., Ishizuka, S., Kitamura, K., Jeong, J., Sato, M., Hinata, N., and Abe, S. (2020). Morphological association between the muscles and bones in the craniofacial region. PLoS One *15*, e0227301. 10.1371/journal.pone.0227301.
72. Shen, H., Grimston, S., Civitelli, R., and Thomopoulos, S. (2015). Deletion of connexin43 in osteoblasts/osteocytes leads to impaired muscle formation in mice. J Bone Miner Res *30*, 596-605. 10.1002/jbmr.2389.
73. Kitai, N., Fujii, Y., Murakami, S., Furukawa, S., Kreiborg, S., and Takada, K. (2002). Human masticatory muscle volume and zygomatico-mandibular form in adults with mandibular prognathism. J Dent Res *81*, 752-756. 10.1177/0810752.
74. Yamamoto, M., Ho Cho, K., Murakami, G., Abe, S., and Rodriguez-Vazquez, J.F. (2018). Early Fetal Development of the Otic and Pterygopalatine Ganglia with Special Reference to the Topographical Relationship with the Developing Sphenoid Bone. Anat Rec (Hoboken) *301*, 1442-1453. 10.1002/ar.23833.
75. Toth, M., Sirirattanapan, J., and Mann, W. (2013). Patterns of anomalies of structures of the middle ear and the facial nerve as revealed in newborn temporal bones. Otol Neurotol *34*, 1121-1126. 10.1097/MAO.0b013e318283987f.
76. Iyyanar, P.P.R., Wu, Z., Lan, Y., Hu, Y.C., and Jiang, R. (2022). Alx1 Deficient Mice Recapitulate Craniofacial Phenotype and Reveal Developmental Basis of ALX1-Related Frontonasal Dysplasia. Front Cell Dev Biol *10*, 777887. 10.3389/fcell.2022.777887.
77. Dai, X.-M., Zong, X.-H., Akhter, M.P., and Stanley, E.R. (2004). Osteoclast Deficiency Results in Disorganized Matrix, Reduced Mineralization, and Abnormal Osteoblast

1034 Behavior in Developing Bone. Journal of Bone and Mineral Research *19*, 1441-1451.
1035 https://doi.org/10.1359/JBMR.040514.
1036 78. Harris, S.E., MacDougall, M., Horn, D., Woodruff, K., Zimmer, S.N., Rebel, V.I.,
1037 Fajardo, R., Feng, J.Q., Gluhak-Heinrich, J., Harris, M.A., and Abboud Werner, S.
1038 (2012). Meox2Cre-mediated disruption of CSF-1 leads to osteopetrosis and osteocyte
1039 defects. Bone *50*, 42-53. 10.1016/j.bone.2011.09.038.
1040 79. Ryan, G.R., Dai, X.M., Dominguez, M.G., Tong, W., Chuan, F., Chisholm, O., Russell,
1041 R.G., Pollard, J.W., and Stanley, E.R. (2001). Rescue of the colony-stimulating factor 1
1042 (CSF-1)-nullizygous mouse (Csf1(op)/Csf1(op)) phenotype with a CSF-1 transgene and
1043 identification of sites of local CSF-1 synthesis. Blood *98*, 74-84. 10.1182/blood.v98.1.74.
1044 80. Lawrence, A.R., Canzi, A., Bridlance, C., Olivie, N., Lansonneur, C., Catale, C.,
1045 Pizzamiglio, L., Kloeckner, B., Silvin, A., Munro, D.A.D., et al. (2024). Microglia
1046 maintain structural integrity during fetal brain morphogenesis. Cell *187*, 962-980 e919.
1047 10.1016/j.cell.2024.01.012.
1048 81. Beerepoot, S., Verbeke, J., Plantinga, M., Nierkens, S., Pouwels, P.J.W., Wolf, N.I.,
1049 Simons, C., and van der Knaap, M.S. (2024). Leukoencephalopathy with calcifications,
1050 developmental brain abnormalities and skeletal dysplasia due to homozygosity for a
1051 hypomorphic CSF1R variant: A report of three siblings. Am J Med Genet A *194*, e63800.
1052 10.1002/ajmg.a.63800.
1053 82. Jiang, J., Li, W., Wang, X., Du, Z., Chen, J., Liu, Y., Li, W., Lu, Z., Wang, Y., and Xu, J.
1054 (2022). Two Novel Intronic Mutations in the CSF1R Gene in Two Families With CSF1R-
1055 Microglial Encephalopathy. Front Cell Dev Biol *10*, 902067. 10.3389/fcell.2022.902067.
1056 83. Kindis, E., Simsek-Kiper, P.O., Kosukcu, C., Taskiran, E.Z., Gocmen, R., Utine, E.,
1057 Haliloglu, G., Boduroglu, K., and Alikasifoglu, M. (2021). Further expanding the
1058 mutational spectrum of brain abnormalities, neurodegeneration, and dysosteosclerosis: A
1059 rare disorder with neurologic regression and skeletal features. Am J Med Genet A *185*,
1060 1888-1896. 10.1002/ajmg.a.62179.
1061 84. Oosterhof, N., Chang, I.J., Karimiani, E.G., Kuil, L.E., Jensen, D.M., Daza, R., Young,
1062 E., Astle, L., van der Linde, H.C., Shivaram, G.M., et al. (2019). Homozygous Mutations
1063 in CSF1R Cause a Pediatric-Onset Leukoencephalopathy and Can Result in Congenital
1064 Absence of Microglia. The American Journal of Human Genetics *104*, 936-947.
1065 https://doi.org/10.1016/j.ajhg.2019.03.010.
1066 85. Oosterhof, N., Kuil, L.E., van der Linde, H.C., Burm, S.M., Berdowski, W., van Ijcken,
1067 W.F.J., van Swieten, J.C., Hol, E.M., Verheijen, M.H.G., and van Ham, T.J. (2018).
1068 Colony-Stimulating Factor 1 Receptor (CSF1R) Regulates Microglia Density and
1069 Distribution, but Not Microglia Differentiation In Vivo. Cell Rep *24*, 1203-1217 e1206.
1070 10.1016/j.celrep.2018.06.113.
1071 86. Tamhankar, P.M., Zhu, B., Tamhankar, V.P., Mithbawkar, S., Seabra, L., Livingston, J.H.,
1072 Ikeuchi, T., and Crow, Y.J. (2020). A Novel Hypomorphic CSF1R Gene Mutation in the
1073 Biallelic State Leading to Fatal Childhood Neurodegeneration. Neuropediatrics *51*, 302-
1074 306. 10.1055/s-0040-1702161.
1075 87. Daghagh, H., Rahbar Kafshboran, H., Daneshmandpour, Y., Nasiri Aghdam, M.,
1076 Talebian, S., Nouri Nojadeh, J., Hamzeiy, H., Biskup, S., and Sakhinia, E. (2023).
1077 Homozygous mutation in CSF1R causes brain abnormalities, neurodegeneration, and
1078 dysosteosclerosis (BANDDOS). Bioimpacts *13*, 183-190. 10.34172/bi.2022.23528.

1079 88. Dulski, J., Souza, J., Santos, M.L., and Wszolek, Z.K. (2023). Brain abnormalities,
1080 neurodegeneration, and dysosteosclerosis (BANDDOS): new cases, systematic literature
1081 review, and associations with CSF1R-ALSP. Orphanet J Rare Dis *18*, 160.
1082 10.1186/s13023-023-02772-9.
1083 89. Inoue, K., Qin, Y., Xia, Y., Han, J., Yuan, R., Sun, J., Xu, R., Jiang, J.X., Greenblatt,
1084 M.B., and Zhao, B. (2023). Bone marrow Adipoq-lineage progenitors are a major cellular
1085 source of M-CSF that dominates bone marrow macrophage development,
1086 osteoclastogenesis, and bone mass. Elife *12*. 10.7554/eLife.82118.
1087 90. Nandi, S., Akhter, M.P., Seifert, M.F., Dai, X.M., and Stanley, E.R. (2006).
1088 Developmental and functional significance of the CSF-1 proteoglycan chondroitin sulfate
1089 chain. Blood *107*, 786-795. 10.1182/blood-2005-05-1822.
1090 91. Batoon, L., Keshvari, S., Irvine, K.M., Ho, E., Caruso, M., Patkar, O.L., Sehgal, A.,
1091 Millard, S.M., Hume, D.A., and Pettit, A.R. (2024). Relative contributions of osteal
1092 macrophages and osteoclasts to postnatal bone development in CSF1R-deficient rats and
1093 phenotype rescue following wild-type bone marrow cell transfer. J Leukoc Biol *116*, 753-
1094 765. 10.1093/jleuko/qiae077.
1095 92. Batoon, L., Millard, S.M., Wullschleger, M.E., Preda, C., Wu, A.C., Kaur, S., Tseng,
1096 H.W., Hume, D.A., Levesque, J.P., Raggatt, L.J., and Pettit, A.R. (2019). CD169(+)
1097 macrophages are critical for osteoblast maintenance and promote intramembranous and
1098 endochondral ossification during bone repair. Biomaterials *196*, 51-66.
1099 10.1016/j.biomaterials.2017.10.033.
1100 93. Alexander, K.A., Chang, M.K., Maylin, E.R., Kohler, T., Muller, R., Wu, A.C., Van
1101 Rooijen, N., Sweet, M.J., Hume, D.A., Raggatt, L.J., and Pettit, A.R. (2011). Osteal
1102 macrophages promote in vivo intramembranous bone healing in a mouse tibial injury
1103 model. J Bone Miner Res *26*, 1517-1532. 10.1002/jbmr.354.
1104 94. Blumer, M.J., Longato, S., and Fritsch, H. (2008). Localization of tartrate-resistant acid
1105 phosphatase (TRAP), membrane type-1 matrix metalloproteinases (MT1-MMP) and
1106 macrophages during early endochondral bone formation. J Anat *213*, 431-441.
1107 10.1111/j.1469-7580.2008.00958.x.
1108 95. Chang, M.K., Raggatt, L.J., Alexander, K.A., Kuliwaba, J.S., Fazzalari, N.L., Schroder,
1109 K., Maylin, E.R., Ripoll, V.M., Hume, D.A., and Pettit, A.R. (2008). Osteal tissue
1110 macrophages are intercalated throughout human and mouse bone lining tissues and
1111 regulate osteoblast function in vitro and in vivo. J Immunol *181*, 1232-1244.
1112 10.4049/jimmunol.181.2.1232.
1113 96. Batoon, L., Koh, A.J., Millard, S.M., Grewal, J., Choo, F.M., Kannan, R., Kinnaird, A.,
1114 Avey, M., Teslya, T., Pettit, A.R., et al. (2024). Induction of osteoblast apoptosis
1115 stimulates macrophage efferocytosis and paradoxical bone formation. Bone Res *12*, 43.
1116 10.1038/s41413-024-00341-9.
1117 97. Poli, V., Balena, R., Fattori, E., Markatos, A., Yamamoto, M., Tanaka, H., Ciliberto, G.,
1118 Rodan, G.A., and Costantini, F. (1994). Interleukin-6 deficient mice are protected from
1119 bone loss caused by estrogen depletion. EMBO J *13*, 1189-1196. 10.1002/j.1460-
1120 2075.1994.tb06368.x.
1121 98. Jilka, R.L., Hangoc, G., Girasole, G., Passeri, G., Williams, D.C., Abrams, J.S., Boyce,
1122 B., Broxmeyer, H., and Manolagas, S.C. (1992). Increased osteoclast development after
1123 estrogen loss: mediation by interleukin-6. Science *257*, 88-91. 10.1126/science.1621100.

1124 99. Mun, S.H., Jastrzebski, S., Kalinowski, J., Zeng, S., Oh, B., Bae, S., Eugenia, G., Khan,
1125 N.M., Drissi, H., Zhou, P., et al. (2021). Sexual Dimorphism in Differentiating Osteoclast
1126 Precursors Demonstrates Enhanced Inflammatory Pathway Activation in Female Cells. J
1127 Bone Miner Res *36*, 1104-1116. 10.1002/jbmr.4270.
1128 100. Herbert, B.A., Valerio, M.S., Gaestel, M., and Kirkwood, K.L. (2015). Sexual
1129 Dimorphism in MAPK-Activated Protein Kinase-2 (MK2) Regulation of RANKL-
1130 Induced Osteoclastogenesis in Osteoclast Progenitor Subpopulations. PLoS One *10*,
1131 e0125387. 10.1371/journal.pone.0125387.
1132 101. Paglia, D.N., Yang, X., Kalinowski, J., Jastrzebski, S., Drissi, H., and Lorenzo, J. (2016).
1133 Runx1 Regulates Myeloid Precursor Differentiation Into Osteoclasts Without Affecting
1134 Differentiation Into Antigen Presenting or Phagocytic Cells in Both Males and Females.
1135 Endocrinology *157*, 3058-3069. 10.1210/en.2015-2037.
1136 102. Cenci, S., Weitzmann, M.N., Roggia, C., Namba, N., Novack, D., Woodring, J., and
1137 Pacifici, R. (2000). Estrogen deficiency induces bone loss by enhancing T-cell production
1138 of TNF-alpha. J Clin Invest *106*, 1229-1237. 10.1172/JCI11066.
1139 103. Kimble, R.B., Srivastava, S., Ross, F.P., Matayoshi, A., and Pacifici, R. (1996). Estrogen
1140 deficiency increases the ability of stromal cells to support murine osteoclastogenesis via
1141 an interleukin-1and tumor necrosis factor-mediated stimulation of macrophage colony-
1142 stimulating factor production. J Biol Chem *271*, 28890-28897. 10.1074/jbc.271.46.28890.
1143 104. Srivastava, S., Weitzmann, M.N., Kimble, R.B., Rizzo, M., Zahner, M., Milbrandt, J.,
1144 Ross, F.P., and Pacifici, R. (1998). Estrogen blocks M-CSF gene expression and
1145 osteoclast formation by regulating phosphorylation of Egr-1 and its interaction with Sp-1.
1146 J Clin Invest *102*, 1850-1859. 10.1172/JCI4561.
1147 105. Przystanska, A., Rewekant, A., Sroka, A., Gedrange, T., Ekkert, M., Jonczyk-Potoczna,
1148 K., and Czajka-Jakubowska, A. (2020). Sexual dimorphism of maxillary sinuses in
1149 children and adolescents - A retrospective CT study. Ann Anat *229*, 151437.
1150 10.1016/j.aanat.2019.151437.
1151 106. Dixon, J., and Dixon, M.J. (2004). Genetic background has a major effect on the
1152 penetrance and severity of craniofacial defects in mice heterozygous for the gene
1153 encoding the nucleolar protein Treacle. Dev Dyn *229*, 907-914. 10.1002/dvdy.20004.
1154 107. Holmes, G., O'Rourke, C., Motch Perrine, S.M., Lu, N., van Bakel, H., Richtsmeier, J.T.,
1155 and Jabs, E.W. (2018). Midface and upper airway dysgenesis in FGFR2-related
1156 craniosynostosis involves multiple tissue-specific and cell cycle effects. Development
1157 *145*. 10.1242/dev.166488.
1158 108. Motch Perrine, S.M., Stecko, T., Neuberger, T., Jabs, E.W., Ryan, T.M., and Richtsmeier,
1159 J.T. (2017). Integration of Brain and Skull in Prenatal Mouse Models of Apert and
1160 Crouzon Syndromes. Front Hum Neurosci *11*, 369. 10.3389/fnhum.2017.00369.
1161 109. Cobolli Gigli, C., Scaramuzza, L., Gandaglia, A., Bellini, E., Gabaglio, M., Parolaro, D.,
1162 Kilstrup-Nielsen, C., Landsberger, N., and Bedogni, F. (2016). MeCP2 Related Studies
1163 Benefit from the Use of CD1 as Genetic Background. PLoS One *11*, e0153473.
1164 10.1371/journal.pone.0153473.
1165 110. Warren, E.B., Briano, J.A., Ellegood, J., DeYoung, T., Lerch, J.P., and Morrow, E.M.
1166 (2022). 17q12 deletion syndrome mouse model shows defects in craniofacial, brain and
1167 kidney development, and glucose homeostasis. Dis Model Mech *15*.
1168 10.1242/dmm.049752.

111. Yan, J., Bi, W., and Lupski, J.R. (2007). Penetrance of Craniofacial Anomalies in Mouse Models of Smith-Magenis Syndrome Is Modified by Genomic Sequence Surrounding Rai1: Not All Null Alleles Are Alike. The American Journal of Human Genetics *80*, 518-525. 10.1086/512043.
112. Sugiyama, A., and Takigawa, T. (2020). Genetic background influences the capacity for medial edge epithelium disintegration and phenotype of cleft palate in TGFbeta3 knockout mice. J Oral Biosci *62*, 260-266. 10.1016/j.job.2020.06.002.
113. Jin, J.Z., and Ding, J. (2015). Strain-Dependent Gene Expression during Mouse Embryonic Palate Development. J Dev Biol *3*, 2-10. 10.3390/jdb3010002.
114. Hall, B.K. (1988). The Embryonic Development of Bone. American Scientist *76*, 174-181.
115. Marvaso, V., and Bernard, G.W. (1977). Initial intramembraneous osteogenesis in vitro. Am J Anat *149*, 453-468. 10.1002/aja.1001490403.
116. Sandberg, M.M. (1991). Matrix in cartilage and bone development: current views on the function and regulation of major organic components. Ann Med *23*, 207-217. 10.3109/07853899109148050.
117. Takarada, T., Nakazato, R., Tsuchikane, A., Fujikawa, K., Iezaki, T., Yoneda, Y., and Hinoi, E. (2016). Genetic analysis of Runx2 function during intramembranous ossification. Development *143*, 211-218. 10.1242/dev.128793.
118. Zimmermann, B. (1992). Degeneration of osteoblasts involved in intramembranous ossification of fetal rat calvaria. Cell Tissue Res *267*, 75-84. 10.1007/BF00318693.
119. Hall, B.K., and Miyake, T. (2000). All for one and one for all: condensations and the initiation of skeletal development. BioEssays *22*, 138-147. 10.1002/(sici)1521-1878(200002)22:2<138::Aid-bies5>3.0.Co;2-4.
120. Mallo, M. (1998). Embryological and genetic aspects of middle ear development. Int. J. Dev. Biol. *42*, 11-22.
121. Miyake, T., Cameron, A.M., and Hall, B.K. (1996). Stage-specific onset of condensation and matrix deposition for Meckel's and other first arch cartilages in inbred C57BL/6 mice. J Craniofac Genet Dev Biol *16*, 32-47.
122. Wood, J.L., Hughes, A.J., Mercer, K.J., and Chapman, S.C. (2010). Analysis of chick (Gallus gallus) middle ear columella formation. BMC Dev Biol *10*, 16. 10.1186/1471-213X-10-16.
123. Chai, Y., Jiang, X., Ito, Y., Bringas, P., Jr., Han, J., Rowitch, D.H., Soriano, P., McMahon, A.P., and Sucov, H.M. (2000). Fate of the mammalian cranial neural crest during tooth and mandibular morphogenesis. Development *127*, 1671-1679. 10.1242/dev.127.8.1671.
124. Jiang, X., Iseki, S., Maxson, R.E., Sucov, H.M., and Morriss-Kay, G.M. (2002). Tissue origins and interactions in the mammalian skull vault. Dev Biol *241*, 106-116. 10.1006/dbio.2001.0487.
125. Jaenisch, R. (1985). Mammalian neural crest cells participate in normal embryonic development on microinjection into post-implantation mouse embryos. Nature *318*, 181-183. 10.1038/318181a0.
126. Tan, S.S., and Morriss-Kay, G.M. (1986). Analysis of cranial neural crest cell migration and early fates in postimplantation rat chimaeras. Development *98*, 21-58. 10.1242/dev.98.1.21.

1213 127. Yoshida, T., Vivatbutsiri, P., Morriss-Kay, G., Saga, Y., and Iseki, S. (2008). Cell lineage
1214 in mammalian craniofacial mesenchyme. Mech Dev *125*, 797-808.
1215 10.1016/j.mod.2008.06.007.
1216 128. Bildsoe, H., Loebel, D.A., Jones, V.J., Hor, A.C., Braithwaite, A.W., Chen, Y.T.,
1217 Behringer, R.R., and Tam, P.P. (2013). The mesenchymal architecture of the cranial
1218 mesoderm of mouse embryos is disrupted by the loss of Twist1 function. Dev Biol *374*,
1219 295-307. 10.1016/j.ydbio.2012.12.004.
1220 129. Dixon, J., Jones, N.C., Sandell, L.L., Jayasinghe, S.M., Crane, J., Rey, J.-P., Dixon, M.J.,
1221 and Trainor, P.A. (2006). *Tcof1*/Treacle is required for neural crest cell formation and
1222 proliferation deficiencies that cause craniofacial abnormalities. Proceedings of the
1223 National Academy of Sciences *103*, 13403-13408. doi:10.1073/pnas.0603730103.
1224 130. Barlow, A.J., and Francis-West, P.H. (1997). Ectopic application of recombinant BMP-2
1225 and BMP-4 can change patterning of developing chick facial primordia. Development
1226 *124*, 391-398. 10.1242/dev.124.2.391.
1227 131. Dixon, J., Brakebusch, C., Fassler, R., and Dixon, M.J. (2000). Increased levels of
1228 apoptosis in the prefusion neural folds underlie the craniofacial disorder, Treacher Collins
1229 syndrome. Hum Mol Genet *9*, 1473-1480. 10.1093/hmg/9.10.1473.
1230 132. Jones, N.C., Lynn, M.L., Gaudenz, K., Sakai, D., Aoto, K., Rey, J.P., Glynn, E.F.,
1231 Ellington, L., Du, C., Dixon, J., et al. (2008). Prevention of the neurocristopathy Treacher
1232 Collins syndrome through inhibition of p53 function. Nat Med *14*, 125-133.
1233 10.1038/nm1725.
1234 133. Richter, C.A., Amin, S., Linden, J., Dixon, J., Dixon, M.J., and Tucker, A.S. (2010).
1235 Defects in middle ear cavitation cause conductive hearing loss in the Tcof1 mutant
1236 mouse. Hum Mol Genet *19*, 1551-1560. 10.1093/hmg/ddq028.
1237 134. D'Amico-Martel, A., and Noden, D.M. (1983). Contributions of placodal and neural crest
1238 cells to avian cranial peripheral ganglia. Am J Anat *166*, 445-468.
1239 10.1002/aja.1001660406.
1240 135. Forbes, D.J., and Welt, C. (1981). Neurogenesis in the trigeminal ganglion of the albino
1241 rat: a quantitative autoradiographic study. J Comp Neurol *199*, 133-147.
1242 10.1002/cne.901990111.
1243 136. Tamura, Y., Matsumura, K., Sano, M., Tabata, H., Kimura, K., Ieda, M., Arai, T., Ohno,
1244 Y., Kanazawa, H., Yuasa, S., et al. (2011). Neural crest-derived stem cells migrate and
1245 differentiate into cardiomyocytes after myocardial infarction. Arterioscler Thromb Vasc
1246 Biol *31*, 582-589. 10.1161/ATVBAHA.110.214726.
1247 137. Kamalakar, A., McKinney, J.M., Salinas Duron, D., Amanso, A.M., Ballestas, S.A.,
1248 Drissi, H., Willett, N.J., Bhattaram, P., Garcia, A.J., Wood, L.B., and Goudy, S.L. (2021).
1249 JAGGED1 stimulates cranial neural crest cell osteoblast commitment pathways and bone
1250 regeneration independent of canonical NOTCH signaling. Bone *143*, 115657.
1251 10.1016/j.bone.2020.115657.
1252 138. Hardaway, A.L., Herroon, M.K., Rajagurubandara, E., and Podgorski, I. (2015). Marrow
1253 adipocyte-derived CXCL1 and CXCL2 contribute to osteolysis in metastatic prostate
1254 cancer. Clin Exp Metastasis *32*, 353-368. 10.1007/s10585-015-9714-5.
1255 139. Hu, Y., Wang, L., Zhao, Z., Lu, W., Fan, J., Gao, B., Luo, Z., Jie, Q., Shi, X., and Yang, L.
1256 (2020). Cytokines CCL2 and CXCL1 may be potential novel predictors of early bone
1257 loss. Mol Med Rep *22*, 4716-4724. 10.3892/mmr.2020.11543.

1258 140. Onan, D., Allan, E.H., Quinn, J.M., Gooi, J.H., Pompolo, S., Sims, N.A., Gillespie, M.T.,
1259 and Martin, T.J. (2009). The chemokine Cxcl1 is a novel target gene of parathyroid
1260 hormone (PTH)/PTH-related protein in committed osteoblasts. Endocrinology *150*, 2244-
1261 2253. 10.1210/en.2008-1597.
1262 141. Miyamoto, K., Ninomiya, K., Sonoda, K.H., Miyauchi, Y., Hoshi, H., Iwasaki, R.,
1263 Miyamoto, H., Yoshida, S., Sato, Y., Morioka, H., et al. (2009). MCP-1 expressed by
1264 osteoclasts stimulates osteoclastogenesis in an autocrine/paracrine manner. Biochem
1265 Biophys Res Commun *383*, 373-377. 10.1016/j.bbrc.2009.04.020.
1266 142. Sul, O.J., Ke, K., Kim, W.K., Kim, S.H., Lee, S.C., Kim, H.J., Kim, S.Y., Suh, J.H., and
1267 Choi, H.S. (2012). Absence of MCP-1 leads to elevated bone mass via impaired actin ring
1268 formation. J Cell Physiol *227*, 1619-1627. 10.1002/jcp.22879.
1269 143. Tamasi, J.A., Vasilov, A., Shimizu, E., Benton, N., Johnson, J., Bitel, C.L., Morrison, N.,
1270 and Partridge, N.C. (2013). Monocyte chemoattractant protein-1 is a mediator of the
1271 anabolic action of parathyroid hormone on bone. J Bone Miner Res *28*, 1975-1986.
1272 10.1002/jbmr.1933.
1273 144. Hoshino, A., Iimura, T., Ueha, S., Hanada, S., Maruoka, Y., Mayahara, M., Suzuki, K.,
1274 Imai, T., Ito, M., Manome, Y., et al. (2010). Deficiency of chemokine receptor CCR1
1275 causes osteopenia due to impaired functions of osteoclasts and osteoblasts. J Biol Chem
1276 *285*, 28826-28837. 10.1074/jbc.M109.099424.
1277 145. Lee, D., Shin, K.J., Kim, D.W., Yoon, K.A., Choi, Y.J., Lee, B.N.R., and Cho, J.Y.
1278 (2018). CCL4 enhances preosteoclast migration and its receptor CCR5 downregulation
1279 by RANKL promotes osteoclastogenesis. Cell Death Dis *9*, 495. 10.1038/s41419-018-
1280 0562-5.
1281 146. Taddei, S.R., Queiroz-Junior, C.M., Moura, A.P., Andrade, I., Jr., Garlet, G.P., Proudfoot,
1282 A.E., Teixeira, M.M., and da Silva, T.A. (2013). The effect of CCL3 and CCR1 in bone
1283 remodeling induced by mechanical loading during orthodontic tooth movement in mice.
1284 Bone *52*, 259-267. 10.1016/j.bone.2012.09.036.
1285 147. Wintges, K., Beil, F.T., Albers, J., Jeschke, A., Schweizer, M., Claass, B., Tiegs, G.,
1286 Amling, M., and Schinke, T. (2013). Impaired bone formation and increased
1287 osteoclastogenesis in mice lacking chemokine (C-C motif) ligand 5 (Ccl5). J Bone Miner
1288 Res *28*, 2070-2080. 10.1002/jbmr.1937.
1289 148. Yu, D., Zhang, S., Ma, C., Huang, S., Xu, L., Liang, J., Li, H., Fan, Q., Liu, G., and Zhai,
1290 Z. (2023). CCL3 in the bone marrow microenvironment causes bone loss and bone
1291 marrow adiposity in aged mice. JCI Insight *8*. 10.1172/jci.insight.159107.
1292 149. Araujo-Pires, A.C., Vieira, A.E., Francisconi, C.F., Biguetti, C.C., Glowacki, A.,
1293 Yoshizawa, S., Campanelli, A.P., Trombone, A.P., Sfeir, C.S., Little, S.R., and Garlet, G.P.
1294 (2015). IL-4/CCL22/CCR4 axis controls regulatory T-cell migration that suppresses
1295 inflammatory bone loss in murine experimental periodontitis. J Bone Miner Res *30*, 412-
1296 422. 10.1002/jbmr.2376.
1297 150. Ha, J., Choi, H.S., Lee, Y., Kwon, H.J., Song, Y.W., and Kim, H.H. (2010). CXC
1298 chemokine ligand 2 induced by receptor activator of NF-kappa B ligand enhances
1299 osteoclastogenesis. J Immunol *184*, 4717-4724. 10.4049/jimmunol.0902444.
1300 151. Ha, J., Lee, Y., and Kim, H.H. (2011). CXCL2 mediates lipopolysaccharide-induced
1301 osteoclastogenesis in RANKL-primed precursors. Cytokine *55*, 48-55.
1302 10.1016/j.cyto.2011.03.026.

1303 152. Ma, C., Gao, J., Liang, J., Wang, F., Xu, L., Bu, J., He, B., Liu, G., Niu, R., and Liu, G.
1304 (2023). CCL12 induces trabecular bone loss by stimulating RANKL production in
1305 BMSCs during acute lung injury. Exp Mol Med *55*, 818-830. 10.1038/s12276-023-
1306 00970-w.
1307 153. Yang, Y., Zhou, X., Li, Y., Chen, A., Liang, W., Liang, G., Huang, B., Li, Q., and Jin, D.
1308 (2019). CXCL2 attenuates osteoblast differentiation by inhibiting the ERK1/2 signaling
1309 pathway. J Cell Sci *132*. 10.1242/jcs.230490.
1310 154. Yano, S., Mentaverri, R., Kanuparthi, D., Bandyopadhyay, S., Rivera, A., Brown, E.M.,
1311 and Chattopadhyay, N. (2005). Functional expression of beta-chemokine receptors in
1312 osteoblasts: role of regulated upon activation, normal T cell expressed and secreted
1313 (RANTES) in osteoblasts and regulation of its secretion by osteoblasts and osteoclasts.
1314 Endocrinology *146*, 2324-2335. 10.1210/en.2005-0065.
1315 155. Kwak, H.B., Ha, H., Kim, H.N., Lee, J.H., Kim, H.S., Lee, S., Kim, H.M., Kim, J.Y.,
1316 Kim, H.H., Song, Y.W., and Lee, Z.H. (2008). Reciprocal cross-talk between RANKL
1317 and interferon-gamma-inducible protein 10 is responsible for bone-erosive experimental
1318 arthritis. Arthritis Rheum *58*, 1332-1342. 10.1002/art.23372.
1319 156. Lee, J.H., Kim, B., Jin, W.J., Kim, H.H., Ha, H., and Lee, Z.H. (2017). Pathogenic roles
1320 of CXCL10 signaling through CXCR3 and TLR4 in macrophages and T cells: relevance
1321 for arthritis. Arthritis Res Ther *19*, 163. 10.1186/s13075-017-1353-6.
1322 157. Marahleh, A., Kitaura, H., Ohori, F., Kishikawa, A., Ogawa, S., Shen, W.R., Qi, J.,
1323 Noguchi, T., Nara, Y., and Mizoguchi, I. (2019). TNF-alpha Directly Enhances Osteocyte
1324 RANKL Expression and Promotes Osteoclast Formation. Front Immunol *10*, 2925.
1325 10.3389/fimmu.2019.02925.
1326 158. Takahashi, T., Wada, T., Mori, M., Kokai, Y., and Ishii, S. (1996). Overexpression of the
1327 granulocyte colony-stimulating factor gene leads to osteoporosis in mice. Lab Invest *74*,
1328 827-834.
1329 159. Takayanagi, H., Kim, S., Matsuo, K., Suzuki, H., Suzuki, T., Sato, K., Yokochi, T., Oda,
1330 H., Nakamura, K., Ida, N., et al. (2002). RANKL maintains bone homeostasis through c-
1331 Fos-dependent induction of interferon-beta. Nature *416*, 744-749. 10.1038/416744a.
1332 160. Yu, H., Zhang, T., Lu, H., Ma, Q., Zhao, D., Sun, J., and Wang, Z. (2021). Granulocyte
1333 colony-stimulating factor (G-CSF) mediates bone resorption in periodontitis. BMC Oral
1334 Health *21*, 299. 10.1186/s12903-021-01658-1.
1335 161. Zhang, Y.H., Heulsmann, A., Tondravi, M.M., Mukherjee, A., and Abu-Amer, Y. (2001).
1336 Tumor necrosis factor-alpha (TNF) stimulates RANKL-induced osteoclastogenesis via
1337 coupling of TNF type 1 receptor and RANK signaling pathways. J Biol Chem *276*, 563-
1338 568. 10.1074/jbc.M008198200.
1339 162. Zhao, R., Chen, N.N., Zhou, X.W., Miao, P., Hu, C.Y., Qian, L., Yu, Q.W., Zhang, J.Y.,
1340 Nie, H., Chen, X.H., et al. (2014). Exogenous IFN-beta regulates the RANKL-c-Fos-IFN-
1341 beta signaling pathway in the collagen antibody-induced arthritis model. J Transl Med *12*,
1342 330. 10.1186/s12967-014-0330-y.
1343 163. Kaneshiro, S., Ebina, K., Shi, K., Higuchi, C., Hirao, M., Okamoto, M., Koizumi, K.,
1344 Morimoto, T., Yoshikawa, H., and Hashimoto, J. (2014). IL-6 negatively regulates
1345 osteoblast differentiation through the SHP2/MEK2 and SHP2/Akt2 pathways in vitro. J
1346 Bone Miner Metab *32*, 378-392. 10.1007/s00774-013-0514-1.
1347 164. Kitamura, H., Kawata, H., Takahashi, F., Higuchi, Y., Furuichi, T., and Ohkawa, H.
1348 (1995). Bone marrow neutrophilia and suppressed bone turnover in human interleukin-6

transgenic mice. A cellular relationship among hematopoietic cells, osteoblasts, and osteoclasts mediated by stromal cells in bone marrow. Am J Pathol *147*, 1682-1692.

165. Liu, H., Feng, W., Yimin, Cui, J., Lv, S., Hasegawa, T., Sun, B., Li, J., Oda, K., Amizuka, N., and Li, M. (2014). Histological Evidence of Increased Osteoclast Cell Number and Asymmetric Bone Resorption Activity in the Tibiae of Interleukin-6-Deficient Mice. J Histochem Cytochem *62*, 556-564. 10.1369/0022155414537830.

166. Palmqvist, P., Persson, E., Conaway, H.H., and Lerner, U.H. (2002). IL-6, leukemia inhibitory factor, and oncostatin M stimulate bone resorption and regulate the expression of receptor activator of NF-kappa B ligand, osteoprotegerin, and receptor activator of NF-kappa B in mouse calvariae. J Immunol *169*, 3353-3362. 10.4049/jimmunol.169.6.3353.

167. Hayden, J.M., Mohan, S., and Baylink, D.J. (1995). The insulin-like growth factor system and the coupling of formation to resorption. Bone *17*, 93S-98S. 10.1016/8756-3282(95)00186-h.

168. Howard, G.A., Bottemiller, B.L., Turner, R.T., Rader, J.I., and Baylink, D.J. (1981). Parathyroid hormone stimulates bone formation and resorption in organ culture: evidence for a coupling mechanism. Proc Natl Acad Sci U S A *78*, 3204-3208. 10.1073/pnas.78.5.3204.

169. Nakamura, M., Udagawa, N., Matsuura, S., Mogi, M., Nakamura, H., Horiuchi, H., Saito, N., Hiraoka, B.Y., Kobayashi, Y., Takaoka, K., et al. (2003). Osteoprotegerin regulates bone formation through a coupling mechanism with bone resorption. Endocrinology *144*, 5441-5449. 10.1210/en.2003-0717.

170. Tang, Y., Wu, X., Lei, W., Pang, L., Wan, C., Shi, Z., Zhao, L., Nagy, T.R., Peng, X., Hu, J., et al. (2009). TGF-beta1-induced migration of bone mesenchymal stem cells couples bone resorption with formation. Nat Med *15*, 757-765. 10.1038/nm.1979.

171. Zhao, C., Irie, N., Takada, Y., Shimoda, K., Miyamoto, T., Nishiwaki, T., Suda, T., and Matsuo, K. (2006). Bidirectional ephrinB2-EphB4 signaling controls bone homeostasis. Cell Metab *4*, 111-121. 10.1016/j.cmet.2006.05.012.

172. Hu, Z.L., Shi, M., Huang, Y., Zheng, M.H., Pei, Z., Chen, J.Y., Han, H., and Ding, Y.Q. (2011). The role of the transcription factor Rbpj in the development of dorsal root ganglia. Neural Dev *6*, 14. 10.1186/1749-8104-6-14.

173. Ngan, E.S., Garcia-Barcelo, M.M., Yip, B.H., Poon, H.C., Lau, S.T., Kwok, C.K., Sat, E., Sham, M.H., Wong, K.K., Wainwright, B.J., et al. (2011). Hedgehog/Notch-induced premature gliogenesis represents a new disease mechanism for Hirschsprung disease in mice and humans. J Clin Invest *121*, 3467-3478. 10.1172/JCI43737.

174. Rabbani, P., Takeo, M., Chou, W., Myung, P., Bosenberg, M., Chin, L., Taketo, M.M., and Ito, M. (2011). Coordinated activation of Wnt in epithelial and melanocyte stem cells initiates pigmented hair regeneration. Cell *145*, 941-955. 10.1016/j.cell.2011.05.004.

175. Wang, Z., Wu, Z., Wang, H., Feng, R., Wang, G., Li, M., Wang, S.Y., Chen, X., Su, Y., Wang, J., et al. (2023). An immune cell atlas reveals the dynamics of human macrophage specification during prenatal development. Cell *186*, 4454-4471 e4419. 10.1016/j.cell.2023.08.019.

176. Eom, D.S., and Parichy, D.M. (2017). A macrophage relay for long-distance signaling during postembryonic tissue remodeling. Science *355*, 1317-1320. 10.1126/science.aal2745.

177. Yang, X., Tang, C., Zhu, D., Xia, X., Du, Q., Huang, L., Liu, J., and Liu, Y. (2025). Nonylphenol exposure increases the risk of Hirschsprung's disease by inducing

macrophage M1 polarization. Ecotoxicol Environ Saf *290*, 117756. 10.1016/j.ecoenv.2025.117756.

178. Brown, L.N., Xing, Y., Noble, K.V., Barth, J.L., Panganiban, C.H., Smythe, N.M., Bridges, M.C., Zhu, J., and Lang, H. (2017). Macrophage-Mediated Glial Cell Elimination in the Postnatal Mouse Cochlea. Front Mol Neurosci *10*, 407. 10.3389/fnmol.2017.00407.

179. McFarlane, L., Truong, V., Palmer, J.S., and Wilhelm, D. (2013). Novel PCR assay for determining the genetic sex of mice. Sex Dev *7*, 207-211. 10.1159/000348677.

180. Tiscornia, G., Singer, O., Ikawa, M., and Verma, I.M. (2003). A general method for gene knockdown in mice by using lentiviral vectors expressing small interfering RNA. Proc Natl Acad Sci U S A *100*, 1844-1848. 10.1073/pnas.0437912100.

181. The Jackson Laboratory. Protocol 29436: Standard PCR Assay - Gt(ROSA)26Sor(tdTomato-WPRE). https://www.jax.org/Protocol?stockNumber=007914&protocolID=29436.

182. The Jackson Laboratory. Protocol 25394: Standard PCR Assay - Tg(Wnt1-cre). https://www.jax.org/Protocol?stockNumber=022501&protocolID=25394.

183. Posit team (2025). RStudio: Integrated Development Environment for R (Posit Software, PBC).

184. R Core Team (2024). R: A Language and Environment for Statistical Computing (R Foundation for Statistical Computing).

185. Hao, Y., Stuart, T., Kowalski, M.H., Choudhary, S., Hoffman, P., Hartman, A., Srivastava, A., Molla, G., Madad, S., Fernandez-Granda, C., and Satija, R. (2024). Dictionary learning for integrative, multimodal and scalable single-cell analysis. Nat Biotechnol *42*, 293-304. 10.1038/s41587-023-01767-y.

186. Hao, Y., Hao, S., Andersen-Nissen, E., Mauck, W.M., 3rd, Zheng, S., Butler, A., Lee, M.J., Wilk, A.J., Darby, C., Zager, M., et al. (2021). Integrated analysis of multimodal single-cell data. Cell *184*, 3573-3587 e3529. 10.1016/j.cell.2021.04.048.

187. Stuart, T., Butler, A., Hoffman, P., Hafemeister, C., Papalexi, E., Mauck, W.M., 3rd, Hao, Y., Stoeckius, M., Smibert, P., and Satija, R. (2019). Comprehensive Integration of Single-Cell Data. Cell *177*, 1888-1902 e1821. 10.1016/j.cell.2019.05.031.

188. Butler, A., Hoffman, P., Smibert, P., Papalexi, E., and Satija, R. (2018). Integrating single-cell transcriptomic data across different conditions, technologies, and species. Nat Biotechnol *36*, 411-420. 10.1038/nbt.4096.

189. Satija, R., Farrell, J.A., Gennert, D., Schier, A.F., and Regev, A. (2015). Spatial reconstruction of single-cell gene expression data. Nat Biotechnol *33*, 495-502. 10.1038/nbt.3192.

190. Schindelin, J., Arganda-Carreras, I., Frise, E., Kaynig, V., Longair, M., Pietzsch, T., Preibisch, S., Rueden, C., Saalfeld, S., Schmid, B., et al. (2012). Fiji: an open-source platform for biological-image analysis. Nat Methods *9*, 676-682. 10.1038/nmeth.2019.

191. Schneider, C.A., Rasband, W.S., and Eliceiri, K.W. (2012). NIH Image to ImageJ: 25 years of image analysis. Nat Methods *9*, 671-675. 10.1038/nmeth.2089.

192. GraphPad Software (2025). GraphPad Prism.

193. Adobe Inc. (2025). Adobe Photoshop.

194. ZEISS Microscopy (2025). ZEISS ZEN Microscopy Software.

195. Beckman Coulter Life Sciences (2025). CytExpert Software.

196. Rosin, J.M., Kurrasch, D.M., and Cobb, J. (2015). Shox2 is required for the proper development of the facial motor nucleus and the establishment of the facial nerves. BMC Neurosci *16*, 39. 10.1186/s12868-015-0176-0.
197. Tosun, B., Wolff, L.I., Houben, A., Nutt, S., and Hartmann, C. (2022). Osteoclasts and Macrophages-Their Role in Bone Marrow Cavity Formation During Mouse Embryonic Development. J Bone Miner Res *37*, 1761-1774. 10.1002/jbmr.4629.
198. Ralphs, J.R. (1992). Chondrogenesis and myogenesis in micromass cultures of mesenchyme from mouse facial primordia. In Vitro Cell Dev Biol *28A*, 369-372. 10.1007/BF02877061.
199. Ueharu, H., Yang, J., Komatsu, Y., and Mishina, Y. (2022). Isolation and Culture of Cranial Neural Crest Cells from the First Branchial Arch of Mice. Bio Protoc *12*, e4371. 10.21769/BioProtoc.4371.
200. Tophkhane, S.S., Fu, K., Verheyen, E.M., and Richman, J.M. (2024). Craniofacial studies in chicken embryos confirm the pathogenicity of human FZD2 variants associated with Robinow syndrome. Dis Model Mech *17*. 10.1242/dmm.050584.
201. Rosin, J.M., Sinha, S., Biernaskie, J., and Kurrasch, D.M. (2021). A subpopulation of embryonic microglia respond to maternal stress and influence nearby neural progenitors. Dev Cell *56*, 1326-1345 e1326. 10.1016/j.devcel.2021.03.018.
202. Hagiwara, K., Obayashi, T., Sakayori, N., Yamanishi, E., Hayashi, R., Osumi, N., Nakazawa, T., and Nishida, K. (2014). Molecular and cellular features of murine craniofacial and trunk neural crest cells as stem cell-like cells. PLoS One *9*, e84072. 10.1371/journal.pone.0084072.
203. Gutiérrez, M.L., Guevara, J., and Barrera, L.A. (2012). Semi-automatic grading system in histologic and immunohistochemistry analysis to evaluate in vitro chondrogenesis. Universitas Scientiarum *17*, 167-178.

1491 **STAR★METHODS**

1492 **KEY RESOURCES TABLE**

REAGENT or RESOURCE	SOURCE	IDENTIFIER
Antibodies		
Sheep polyclonal anti-CSF1R	R&D Systems	Cat#AF3818; RRID: AB_884158
Rabbit polyclonal anti-Cathepsin K	Abcam	Cat#ab19027; RRID: AB_2261274
Rabbit monoclonal anti-Sp7 (clone EPR21034)	Abcam	Cat#ab209484; RRID: AB_2892207
Rabbit monoclonal anti-Active Caspase 3 (clone C92-605)	BD Pharmingen	Cat#559565; RRID: AB_397274
Mouse monoclonal 2H3 (concentrate)	Developmental Studies Hybridoma Bank	Cat#2H3; RRID: AB_531793
Mouse monoclonal MF20 (concentrate)	Developmental Studies Hybridoma Bank	Cat#MF 20; RRID: AB_2147781
Goat polyclonal anti-CCL3	R&D Systems	Cat#AF-450-NA; RRID: AB_354492
Goat polyclonal anti-CCL4	R&D Systems	Cat#AF-451-NA; RRID: AB_2071055
Goat polyclonal anti-PDGFRα	R&D Systems	Cat#AF1062; RRID: AB_2236897
Rabbit polyclonal anti-SOX2	Millipore	Cat#AB5603; RRID: AB_2286686
Mouse monoclonal anti-SOX10 (clone 20B7)	R&D Systems	Cat#MAB2864; RRID: AB_2195180
Mouse monoclonal anti-Ki67 (clone B56)	BD Pharmingen	Cat#556003; RRID: AB_396287
Chemicals, peptides, and recombinant proteins		
Alizarin Red	Sigma-Aldrich	Cat#A5533; CAS: 130-22-3

Alcian Blue	Sigma-Aldrich	Cat#05500; CAS: 33864-99-2
3,3′ -Diaminobenzidine tetrahydrochloride (DAB)	Sigma-Aldrich	Cat#D5905; CAS: 7411-49-6
L-(+)-Tartaric acid	Sigma-Aldrich	Cat#T109; CAS: 87-69-4
Naphthol AS-MX phosphate	Sigma-Aldrich	Cat#N4875; CAS: 1596-56-1
Fast Red Violet LB Salt	Sigma-Aldrich	Cat#F3381; CAS: 32348-81-5
Silver nitrate	Sigma-Aldrich	Cat#209139; CAS: 7761-88-8
Ascorbic acid	Thermo Fisher Scientific	Cat#850-3080IM; CAS: 50-81-7
10 mM β-glycerol phosphate	Sigma-Aldrich	Cat#G9422; CAS: 154804-51-0
Shandon's Instant Hematoxylin	Thermo Fisher Scientific	Cat#6765015
Hoechst 33342	Invitrogen	Cat#H3570; CAS: 23491-52-3
Proteinase K	New England Biolabs	Cat#P8107S; UniProtKB: P06873
OneTaq® Quick-Load® 2X Master Mix with Standard Buffer	New England Biolabs	Cat#M0486S
SmartGlow Pre-stain for nucleic acid gels	Accuris Instruments	Cat#E4500-PS
GeneRuler Ready-to-Use 100BP DNA Ladder	Thermo Fisher Scientific	Cat#SM0243
Human Recombinant Epidermal Growth Factor	STEMCELL Technologies	Cat#78006.1
Human Recombinant Basic Fibroblast Growth Factor	STEMCELL Technologies	Cat#78003.1
Critical commercial assays		
MILLIPLEX® Mouse Cytokine/Chemokine Magnetic Bead Panel - Immunology Multiplex Assay	Millipore	Cat#MCYTOMAG-70K
MILLIPLEX® Mouse Cytokine/Chemokine Magnetic Bead Panel II	Millipore	Cat#MECY2MAG-73K
RNAscope™ Multiplex Fluorescent Reagent Kit v2	Advanced Cell Diagnostics	Cat#323100
TSA Vivid™ fluorophore 520	Advanced Cell Diagnostics	Cat#323271
TSA Vivid™ fluorophore 570	Advanced Cell Diagnostics	Cat#323272

RNAscope™ Probe - Mm-Csf1r-C3	Advanced Cell Diagnostics	Cat#428191-C3
RNAscope™ Probe - Mm-Ccl4	Advanced Cell Diagnostics	Cat#421071
Deposited data		
E12.5 WT mouse cranial tissue single cell RNA sequencing dataset	Angelozzi et al.[54]	GEO: GSM6146223
E13.5 WT mouse cranial tissue single cell RNA sequencing dataset	Angelozzi et al.[54]	GEO: GSM5324643
E12.5 mouse face tissue single cell RNA sequencing dataset	Rajderkar et al.[55]	GEO: GSM7508877
Experimental models: Organisms/strains		
CD1 mice (Crl:CD1(ICR))	Charles River	CR: 022; RRID: IMSR_CRL:022
C57BL/6 mice (C57BL/6NJ)	The Jackson Laboratory	JAX: 005304; RRID: IMSR_JAX:005304
Csf1r^{EGFP} mice (B6.Cg-Tg(Csf1r-EGFP)1Hume/J)	The Jackson Laboratory	JAX: 018549; RRID: IMSR_JAX:018549
Wnt1^{Cre} mice (B6.Cg-*E2f1*$^{Tg(Wnt1\text{-}cre)2Sor}$/J)	The Jackson Laboratory	JAX: 022501; RRID: IMSR_JAX:022501
Rosa26^{tdTomato} mice (B6.Cg-*Gt(ROSA)26Sor*$^{tm14(CAG\text{-}tdTomato)Hze}$/J)	The Jackson Laboratory	JAX: 007914; RRID: IMSR_JAX:007914
Oligonucleotides		
Primers for genotyping. See Table S4 for primer sequences.	McFarlane et al.[179], Tiscornia et al.[180], The Jackson Laboratory[181,182]	N/A
Software and algorithms		
RStudio	Posit team[183]	RRID:SCR_000432; https://posit.co/download/rstudio-desktop/

R Project for Statistical Computing	R Core Team[184]	RRID:SCR_001905; https://cran.r-project.org/
Seurat	Hao et al.[185], Hao et al.[186], Stuart et al.[187], Butler et al.[188], Satija et al.[189]	RRID:SCR_016341; https://cran.r-project.org/web/packages/Seurat/
Fiji	Schindelin et al.[190]	RRID:SCR_002285; https://imagej.net/software/fiji/
ImageJ	Schneider et al.[191]	RRID:SCR_003070; https://imagej.net/software/imagej/
GraphPad Prism	GraphPad Software[192]	RRID:SCR_002798; https://www.graphpad.com/
Adobe Photoshop	Adobe Inc.[193]	RRID:SCR_014199; https://www.adobe.com/products/photoshop.html
ZEISS ZEN Microscopy Software	ZEISS Microscopy[194]	RRID:SCR_013672; https://www.zeiss.com/microscopy/en/products/software/zeiss-zen.html
CytExpert Software	Beckman Coulter Life Sciences[195]	RRID:SCR_017217; https://www.mybeckman.ca/flow-cytometry/research-flow-cytometers/cytoflex/software

EXPERIMENTAL MODEL AND STUDY PARTICIPANT DETAILS

Animal work was carried out in accordance with guidelines and regulations of the Canadian Council of Animal Care and received prior approval from the University of British Columbia's

1497 Animal Care Committee (protocols A21-0170 and A21-0171). CD1 and C57BL/6 embryos and
1498 postnatal day 1 (P1) pups were utilized across the study, as described. *Csf1r*^{EGFP} mice were
1499 crossed to C57BL/6 mice to generate heterozygous embryos for flow cytometry and
1500 immunofluorescence experiments. *Wnt1*^{Cre} mice were crossed to *Rosa26*^{tdTomato} mice to generate
1501 embryos for neural crest-derived sphere culture and for immunofluorescence experiments. Timed
1502 pregnancies were used to collect embryonic samples. For embryonic staging, female mice were
1503 plug-checked in the morning and those with a vaginal plug were assigned embryonic day 0.5
1504 (E0.5). Female mice continued to receive standard chow (LabDiet PicoLab Rodent Diet 20) and
1505 water ad libitum during pregnancy, unless otherwise specified. For embryo collection, pregnant
1506 female mice were anaesthetized with isoflurane and immediately euthanized by cervical
1507 dislocation followed by decapitation. For postnatal staging (i.e., skeletal preparations, μCT
1508 scanning), the day of birth was assigned P0. All mouse embryos and pups were genotyped for
1509 sex and results were reported for both sexes.
1510

1511 **METHOD DETAILS**

1512 **Mouse handling**

1513 Depletion of CSF1R+ cells was achieved by administering the Plexxikon CSF1R inhibitor
1514 PLX5622 (1200 PPM added to chow AIN-76A, Research Diets) to pregnant female mice starting
1515 at E3.5. Control dams received control diet (AIN-76A, Research Diets). Pregnant female mice
1516 were exposed to either control diet or PLX5622 diet from E3.5 until sample collection.
1517 Following birth, female mice were placed on our standard chow (LabDiet PicoLab Rodent Diet
1518 20) from P0 to P1.
1519

1520 **Genotyping**

1521 Tails were collected from all mouse embryos/pups and incubated in extraction buffer (100 mM
1522 NaCl, 50 mM Tris, 100 mM EDTA, 1% SDS) with proteinase K (8 units, ~0.4 mg/mL) overnight
1523 at 56°C. DNA was extracted from digested tails by precipitation with saturated NaCl solution
1524 (~6M), followed by centrifugation at 20,000 g for 10 min. DNA was precipitated from the
1525 supernatant with isopropanol, and pellets were collected by centrifugation at 20,000 g for 5 min.
1526 Pellets were washed with 70% ethanol and dried at 37°C. Dried DNA was dissolved in 200 µL of
1527 Tris-EDTA buffer (10 mM Tris, 1 mM EDTA, pH 8) for 1 h at 68°C, and 1.6 µL of DNA was
1528 subsequently added to OneTaq® Quick-Load® 2X Master Mix with Standard Buffer (New
1529 England Biolabs) along with 1 µM each of primers for SX (*Sly* & *Xlr*), *GFP*, *Wnt1*^{Cre}, or
1530 *Rosa26*^{tdTomato}. PCR reactions were run on a Applied Biosystems™ MiniAmp™ Thermal Cycler
1531 (Applied Biosystems) as follows: 95°C for 3 min, 35 cycles of denaturation at 95°C for 30 sec,
1532 annealing at 60°C (57°C for SX primers) 30 sec, and extension at 72°C for 30 sec, followed by
1533 final extension at 72°C for 5 min. Amplified fragments were run on a 1.5% agarose gel in TAE
1534 buffer (0.4 M Tris, 0.2 M acetic acid, 10 mM EDTA, pH 8) and visualized using SmartGlow Pre-
1535 stain for nucleic acid gels (Accuris Instruments) on a Fisherbrand™ Real Time Electrophoresis
1536 System (Fisher Scientific). DNA fragments were sized according to GeneRuler Ready-to-Use
1537 100bp DNA Ladder (Thermo Fisher Scientific).

1538

1539 **Flow cytometry**

1540 Flow cytometry methods were adapted from Rosin et al[25]. E11.5, 13.5, 15.5, and 17.5 mouse
1541 embryo heads were collected from control and PLX5622-exposed *Csf1r*^{EGFP} mice in PBS on ice.
1542 Craniofacial tissues were then micro-dissected away from the whole head while in PBS on ice.

1543 The micro-dissected craniofacial tissues were cut/dissociated into smaller pieces using a blade
1544 while in culture media on ice containing (v/v): 65.3% DMEM (GIBCO 11965-092, Thermo
1545 Fisher Scientific), 32.7% F-12 (GIBCO 11765-054, Thermo Fisher Scientific), and 2% B-27
1546 supplement (GIBCO 17504-044, Thermo Fisher Scientific). The resulting dissociated tissue was
1547 filtered through a 35 µm strainer (Falcon 352235), placed in a chilled 1.5 mL tube and
1548 centrifuged at 300 g for 5 min at room temperature (RT). The resulting cell pellets were re-
1549 suspended in 500 µL cold HBSS with 5% FBS and filtered through a 35 µm strainer before flow
1550 cytometry. The resulting cell suspensions were analyzed by the University of British Columbia's
1551 Flow Core Facility using a Beckman Coulter Life Sciences CytoFLEX LX machine and
1552 analyzed using Beckman Coulter CytExpert software.
1553
1554 **Tissue section immunohistochemistry**
1555 E15.5 *Csf1r*^{EGFP}, *Wnt1*^{Cre};*Rosa26*^{tdTomato}, and CD1 mouse embryo heads were collected in ice-
1556 cold PBS and fixed in 4% paraformaldehyde (PFA) overnight at 4°C. The tissues were then
1557 washed in PBS and equilibrated in 20% sucrose/PBS overnight at 4°C. Heads were embedded in
1558 Clear Frozen Section Compound (VWR, 95057-838) and cryosectioned (14 µm sections) on a
1559 Leica CM1950 cryostat (Nussloch, Germany). Cryosections were rehydrated in PBS, washed 4 ×
1560 10 min with PBT (PBS with 0.1% Triton X-100), permeabilized for 30 min with 1% Triton X-
1561 100 in PBS, blocked using 5% normal donkey serum (NDS, Sigma) in PBT for 1 h at RT, and
1562 exposed to sheep anti-CSF1R (1:200), rabbit anti-Cathepsin K (1:200), rabbit anti-Active
1563 Caspase 3 (1:500), rabbit anti-Sp7 (1:500), mouse 2H3 (1:200), mouse MF20 (1:100), and/or
1564 mouse anti-Ki67 (1:200) at 4°C overnight. Slides were then washed 4 × 10 min with PBT and
1565 exposed to secondary antibody (1:200, Alexa 488 or Alexa 594 donkey anti-sheep IgG, donkey

1566 anti-rabbit IgG, or donkey anti-mouse IgG, Invitrogen) for 2 h at RT. Nuclei were stained with
1567 1:1000 Hoechst 33342 (Invitrogen) in PBS for 5 min at RT and washed 3 × 5 min with PBT.
1568 Sections were mounted using Aqua Poly/Mount (Polysciences Inc.). Fluorescent images were
1569 captured on a ZEISS Axioplan fluorescent microscope with ZEISS Axiocam HRm camera or a
1570 ZEISS LSM900 confocal microscope and further processed using LSM+. Brightness and/or
1571 contrast of the entire image was adjusted using ZEISS ZEN 3.9 and/or Adobe Photoshop CC if
1572 deemed appropriate.
1573
1574 **Tartrate-resistant acid phosphatase staining**
1575 E15.5 *Csf1r*^{EGFP} mouse embryo head cryosections (described above) were rehydrated in distilled
1576 water and incubated for 30 min at 37°C in pre-warmed TRAP staining solution consisting of 0.1
1577 mg/mL naphthol AS-MX phosphate, 0.6 mg/mL Fast Red Violet LB Salt, 11.4 mg/mL L-(+)
1578 Tartaric Acid, and 9.2 mg/mL sodium acetate anhydrous (Sigma) in 0.28% glacial acetic acid,
1579 with pH adjusted to 4.7–5.0 with 5M sodium hydroxide (Sigma). Slides were then washed with
1580 distilled water, and sections were mounted using Aqua Poly/Mount (Polysciences Inc.). Light
1581 microscope images were captured on a ZEISS Axiocam 208 color camera mounted on a ZEISS
1582 Stemi 508 microscope. Brightness and/or contrast of the entire image was adjusted using Adobe
1583 Photoshop CC if deemed appropriate.
1584
1585 **Whole-mount immunohistochemistry**
1586 Whole-mount staining methods were adapted from Rosin et al[196]. Antibodies recognizing
1587 neurofilament (2H3) and muscle myosin (MF20) were used to visualize embryonic nerves and
1588 muscles. E11.5, 12.5, and 13.5 whole CD1 and C57BL/6 mouse embryos were fixed overnight in

1589 Dent's fixative (4:1, Methanol:DMSO) at 4°C. Embryos were bleached overnight in 5:1 Dent's
1590 fixative:30% H_2O_2 at RT, then rehydrated with successive 30-minute washes in 50%/15%/0%
1591 Methanol in PBS–0.5% Tween 20 (PBST). Embryos were blocked two times for 1 h in PBST/1%
1592 DMSO/2% skim milk powder (PBSTMD) at RT then incubated overnight at 4°C with primary
1593 antibody diluted 1:130–1:150 in PBSTMD to achieve a final concentration of 2 µg/mL. Embryos
1594 were then washed four times for 1 h with PBST, blocked with PBSTMD, and incubated
1595 overnight at 4°C with peroxidase-conjugated goat anti-mouse IgG (Sigma A-9169) diluted 1:300
1596 in PBSTMD, then washed four times for 1 h with PBST, stained with 0.5 mg/mL DAB
1597 (diaminobenzidine) and 0.3% H_2O_2 in PBST, dehydrated to 100% methanol, and cleared in
1598 BABB (1:2, benzyl alcohol:benzyl benzoate). Light microscope images were captured on a
1599 ZEISS Axiocam 208 color camera mounted on a ZEISS Stemi 508 microscope. Brightness
1600 and/or contrast of the entire image was adjusted using Adobe Photoshop CC if deemed
1601 appropriate.
1602
1603 **Von Kossa staining**
1604 Von Kossa staining was adapted from Tosun et al[197]. E15.5 CD1 mouse embryo head
1605 cryosections (described above) were rehydrated in distilled water and incubated in 0.45 µm-
1606 filtered 2% silver-nitrate solution under direct light exposure (14 W, 1500 lumen bulb) for 1 hour,
1607 washed with 1% acetic acid, and subsequently stained for 20 minutes in 0.02% Alcian blue in
1608 70% ethanol and 30% acetic acid. Sections were counterstained in 0.1% Nuclear Fast Red
1609 Solution for 10 minutes and rinsed in distilled water before mounting with Aqua Poly/Mount
1610 (Polysciences Inc.). Slides were imaged on a ZEISS Axiocam 208 color camera mounted on a
1611 ZEISS Stemi 508 microscope.

1612

1613 **Micromass culture**

1614 Micromass culture methods were adapted from Tophkhane et al, Ralphs, and Ueharu et al[198-200].
1615 E12.5 CD1 mouse embryo heads were collected and the frontonasal mass and mandible were
1616 dissected in cold Hank's balanced saline solution (HBSS, without calcium and magnesium;
1617 Thermo Fisher Scientific, #14185052) with 10% FBS and 1% Penicillin/Streptomycin. Dissected
1618 craniofacial tissues were individually incubated in 2% trypsin (Gibco) on ice for 1 h. HBSS with
1619 10% FBS and 1% Penicillin/Streptomycin was added to inhibit the enzymatic activity of trypsin,
1620 pipetting up and down to dissociate the ectoderm and mesenchyme. The cell solution was then
1621 centrifuged at 1000 g for 5 min. The supernatant was removed, and the cells were resuspended in
1622 HBSS with 10% FBS and 1% Penicillin/Streptomycin. The resulting suspension was filtered
1623 through a 35 μm strainer. The mesenchymal cells were counted using a Countess II automated
1624 cell counter (Thermo Fisher Scientific) and were resuspended to 2×10^7 cells/mL in chondrogenic
1625 medium containing 40% DMEM (GIBCO 11995-065, Thermo Fisher Scientific) and 60% F12
1626 (GIBCO 11765-054, Thermo Fisher Scientific) supplemented with 10% FBS, GlutaMAX
1627 (Gibco), 50 μg/mL ascorbic acid (Thermo Fisher Scientific), 10 mM β-glycerol phosphate
1628 (Sigma-Aldrich) and 1% Penicillin/Streptomycin. Cells were dropped into Nunc cell culture-
1629 treated 24-well plates (Thermo Fisher Scientific, Cat#142475) in 10 μL drops at 2×10^5 cells/well
1630 in the center of the well and incubated at 37°C and 5% CO_2 for 90 min to allow cells to attach
1631 and then flooded with 1 mL/well of chondrogenic medium. The culture medium was changed
1632 every other day (days 3, 5, and 7) until day 8. On day 8, cultures were fixed in 4% PFA for 30
1633 min at RT and stored at 4°C in 100 mM Tris (pH 8.3) until staining. Fixed cultures were
1634 incubated at RT in 0.6 mg/mL Fast red violet LB salt and 0.1 mg/mL naphthol AS-MX phosphate

1635 in 100 mM Tris (pH 8.3) for 60 min to stain for alkaline phosphatase activity. The cultures were
1636 then stained with 1% Alcian blue in 3% acetic acid and 1% HCl to detect the area occupied by
1637 cartilage. All cultures were counterstained with 50% Shandon's Instant Hematoxylin (Thermo
1638 Fisher Scientific) and stored in 100% glycerol. Stained cultures were visualized on a ZEISS
1639 Stemi 508 light microscope, and images were captured on a ZEISS Axiocam 208 color camera.
1640

1641 **Bone and cartilage skeletal staining**

1642 P1 CD1 and C57BL/6 mouse pups were collected and sacrificed by decapitation. Eyes were
1643 removed from skinned heads, and heads were then fixed in ethanol with 1% glacial acetic acid
1644 for at least 24 h and placed in 0.45 µm-filtered Alcian blue solution (1 mg/mL Alcian blue 8GX
1645 in 80% ethanol and 20% glacial acetic acid) overnight to stain cartilage. After washing with
1646 ethanol for two 1 h washes, mouse heads were transferred to 1.5% KOH solution for 3.5 h, then
1647 stained with Alizarin Red S solution (0.15 mg/mL Alizarin red S in 0.5% KOH) for 3 h to stain
1648 bone. Skulls were cleared by incubation in 0.5% KOH with 20% glycerol two times for 2–3 days
1649 and stored in a 40% glycerol mixture. Light microscope images were captured on a ZEISS
1650 Axiocam 208 color camera mounted on a ZEISS Stemi 508 microscope. Brightness and/or
1651 contrast of the entire image was adjusted using Adobe Photoshop CC if deemed appropriate.
1652

1653 **Micro-computed tomography (CT)**

1654 P1 CD1 mouse pups were collected and sacrificed by decapitation. Heads were frozen at -20°C
1655 in 15 mL Falcon tubes. For contrast enhanced micro-CT scanning, P1 heads were fixed via
1656 overnight incubation with 4% PFA at 4°C. The samples were then dehydrated through serial
1657 incubations with increasing methanol concentrations (30%, 50% and 70%) in PBS.

1658 Subsequently, samples were incubated in a 1% phosphotungstic acid (PTA)/90% methanol
1659 solution for 2 weeks, ending with rehydration through serial incubations with decreasing
1660 methanol concentrations (70%, 50% and 30%). Incubation with each methanol concentration at
1661 both the dehydration and rehydration steps was done for 2 days. Micro-CT scans were performed
1662 with the Scanco Medical μCT100 scanner at 55 kVp and 200 μA in the Centre for High-
1663 Throughput Phenogenomics at the University of British Columbia. PTA-stained specimens were
1664 scanned at 7 μm resolution while embedded in 1% agarose. Additionally, unstained heads were
1665 micro-CT scanned after thawing at RT for 1 hour, at 15 μm resolution while embedded in 1%
1666 agarose. All outputs were exported as DICOM files.
1667
1668 **Craniofacial tissue culture for cytokine and chemokine analysis**
1669 Methods for tissue culture for cytokine/chemokine analysis were adapted from Rosin et al[201].
1670 E13.5 C57BL/6 mouse embryo heads were collected in PBS at RT. Craniofacial tissues were
1671 then micro-dissected away from the whole head and placed in a cell culture dish with 400 μL of
1672 37°C culture media containing (v/v): 65.3% DMEM, 32.7% F-12, and 2% B27 supplement.
1673 Craniofacial tissues were cultured in a humid incubator with ambient oxygen and 5% CO_2 at
1674 37 °C for 6 h. Culture media was collected and spun down at 3000 g for 10 min at RT, then
1675 supernatant was collected into a new tube, flash frozen, and stored at -75°C until sent for
1676 multiplexed quantification of 45 mouse cytokines, chemokines, and growth factors using
1677 Luminex xMAP technology with MILLIPLEX® Mouse Cytokine/Chemokine Magnetic Bead
1678 Panel and MILLIPLEX® Mouse Cytokine/Chemokine Magnetic Bead Panel II (Millipore),
1679 according to the manufacturer's protocol. The analytes were evaluated on the Luminex™ 200
1680 system (Luminex, Austin, TX, USA) by Eve Technologies Corp. (Calgary, AB, Canada).

1681

1682 **Single-cell RNA sequencing data analysis**

1683 Publicly available single-cell RNA sequencing datasets of wild-type E12.5 and E13.5 C57BL/6J
1684 and FVB/NJ mouse craniofacial mesenchyme were downloaded from the NCBI GEO
1685 database[54,55]. Accession numbers GSM5324643 (E13.5 C57BL/6J), GSM6146223 (E12.5
1686 C57BL/6J), and GSM7508877 (E12.5 FVB/NJ) were imported into Seurat v5 for analysis. Low
1687 quality cells (>20,000 counts, >6,000 genes detected, or >20% mitochondrial genes for
1688 GSM6146223; >35,000 counts, >7,000 genes detected, or >15% mitochondrial genes for
1689 GSM5324643; <1,500 or >7,500 genes detected for GSM7508877) were filtered from
1690 downstream analysis as they may have arisen from damaged cells, multiplets, or other processing
1691 artifacts. Counts were normalized and datasets were filtered to leave only cells with non-zero
1692 *Csf1r* expression. *Csf1r*-expressing cell clusters were identified using graph-based clustering
1693 with the *FindClusters* function, based on variable features and similar cells identified by
1694 *FindNeighbors* function. The *clustree* package was used to assist in determining 0.2 as the
1695 appropriate resolution for clustering, and proper clustering was then verified by manual
1696 inspection of marker genes. Uniform Manifold Approximation and Projections (UMAP) were
1697 visualized using *DimPlot* and gene signatures were visualized using *Vlnplot*. A cluster of
1698 hemoglobin-enriched cells did not express any markers of monocytes, microglia, macrophages,
1699 or osteoclasts except *Csf1r*; this cluster was excluded in the final analysis.

1700

1701 **Fluorescence *in situ* hybridization**

1702 E15.5 CD1 mouse embryo head cryosections (described above) were rehydrated in PBS and
1703 stained according to manufacturer's protocol. Briefly, sections were post-fixed for 15 min at 4°C

1704 in 4% PFA. Slides were then incubated in hydrogen peroxide for 10 min, washed with water, and
1705 incubated in boiling target retrieval buffer for 5 min. Sections were washed with water and
1706 dehydrated in 100% ethanol for 3 min and treated with protease 3 for 30 min at 40°C in a ACD
1707 HybEZ™ II Hybridization System (Advanced Cell Diagnostics). Slides were washed with water
1708 and probes for *Csf1r* (Advanced Cell Diagnostics, Cat#428191-C3) and *Ccl4* (Advanced Cell
1709 Diagnostics, Cat#421071) were hybridized to tissue for 2h at 40°C, followed by incubation in
1710 amplification reagents and TSA Vivid fluorophores, with washes in wash buffer between
1711 incubations. Nuclei were stained with DAPI for 30 seconds and slides were mounted using Aqua
1712 Poly/Mount (Polysciences Inc.). High-resolution images were captured on a ZEISS LSM900
1713 confocal microscope and were further processed using LSM+. Brightness and/or contrast of the
1714 entire image was adjusted using ZEISS ZEN 3.9 and/or Adobe Photoshop CC if deemed
1715 appropriate.
1716
1717 **Neural crest cell sphere culture**
1718 NCC sphere culture methods were adapted from Rosin et al. and Hagiwara et al[201,202]. E12.5
1719 mouse heads were collected (*Wnt1*^{Cre} mice crossed to *Rosa26*^{tdTomato} mice to label neural crest-
1720 derived cells with tdTomato) in 37°C PBS containing 1% Penicillin/Streptomycin. Craniofacial
1721 tissues were then micro-dissected away from the whole head while in PBS containing 1%
1722 Penicillin/Streptomycin. Micro-dissected craniofacial tissues were cut/dissociated into smaller
1723 pieces using a sterile blade. The resulting dissociated tissue was filtered through a 35 µm strainer,
1724 placed in a 1.5 mL tube, and centrifuged at 300 g for 10 min at RT. The resulting cell pellets were
1725 re-suspended in 500 µL of 37 °C warmed culture media containing (v/v): 98% DMEM/F-12 (no
1726 phenol red; GIBCO 21041-025, Thermo Fisher Scientific) and 2% B-27 supplement, with

1727 20 ng/mL each of human recombinant epidermal growth factor and fibroblast growth factor
1728 (STEMCELL Technologies) added. The resulting cell suspensions were filtered through a 35 µm
1729 strainer before fluorescence-activated cell sorting (FACS) by the University of British
1730 Columbia's Flow Core Facility using a Beckman Coulter MoFlo Astrios EQ cell sorter.
1731 tdTomato+ neural crest-derived cells were collected in 500 µL of culture media. Cells were
1732 plated at 12,500 cells/mL per well in 24-well plates and were incubated for 10 days at 37°C with
1733 5% CO_2, with 50% media replenishment at day 5. At day 10, primary spheres were counted and
1734 imaged, dissociated in sterile media, counted, and replated at 1,000 cells/mL and cultured again
1735 for 10 days as above for secondary sphere formation.
1736
1737 **Neural crest sphere immunohistochemistry**
1738 Cultured neural crest-derived spheres (described above) were fixed in 4% PFA for 30 min at RT
1739 and stored in PBS at 4°C until staining. Spheres were washed with PBT (PBS with 0.1% Triton
1740 X-100), blocked using 5% NDS (Sigma) for 1 h at RT, and exposed to goat anti-PDGFRα
1741 (1:150), rabbit anti-SOX2 (1:500) or mouse anti-SOX10 (1:500) at 4°C overnight. Spheres were
1742 then washed with PBT and exposed to secondary antibody (1:200, Alexa 488 donkey anti-goat
1743 IgG, donkey anti-rabbit IgG or donkey anti-mouse IgG, Invitrogen) for 2 h at RT. Nuclei were
1744 stained with Hoechst 33342 (Invitrogen) for 5 min at RT. Spheres were aspirated with a wide
1745 bore pipette tip and deposited onto a glass microscope slide, and were subsequently mounted
1746 using Aqua Poly/Mount (Polysciences Inc.). High-resolution images were captured on a ZEISS
1747 LSM900 with confocal microscope and were further processed using LSM+. Brightness and/or
1748 contrast of the entire image was adjusted using ZEISS ZEN 3.9 and/or Adobe Photoshop CC if
1749 deemed appropriate.

1750

1751 **QUANTIFICATION AND STATISTICAL ANALYSIS**

1752 E15.5 craniofacial tissue sections were obtained by cryosectioning PFA-fixed frozen embryo
1753 heads on a Leica CM1950 cryostat (Nussloch, Germany). Tissue was sectioned coronally starting
1754 from the nose, and 14 µm serial tissue sections were captured across 10 slide sets, with 21
1755 embryonic head sections placed on each slide, and each set comprised of 2 slides. A single set (2
1756 slides) of serial sectioned slides was used for each staining experiment described above. Every
1757 14 µm section containing the craniofacial structure of interest was used for cell counts of cells
1758 with positive expression of *Csf1r*^{EGFP}, CSF1R, cathepsin K, cleaved caspase 3,
1759 *Wnt1*^{Cre}*;Rosa26*^{tdTomato}, and Ki67 (N=3 per sex/treatment from 2-3 dams). For CSF1R, *Csf1r*^{EGFP},
1760 cathepsin K, and cleaved caspase 3 counts, positive cells were counted within the ear, eye,
1761 trigeminal, tongue, and mandible. A 5-cell radius was used for counting cells surrounding the
1762 nasal septum, Meckel's cartilage, and maxillary incisor. For *Wnt1*^{Cre}*;Rosa26*^{tdTomato} counts, the
1763 mineralizing region of the premaxilla and mandible were outlined and cells within this area were
1764 counted. For Ki67 counts, mineralizing areas of the premaxilla and mandible were outlined
1765 comparably to the *Wnt1*^{Cre}*;Rosa26*^{tdTomato} outlines, and Ki67-positive cells within this area were
1766 counted. For micromass alkaline phosphatase staining analysis, images were adjusted by Fiji
1767 v2.16 with ImageJ v1.54 with the *Color Threshold* function using *red, green, and blue (RGB)*
1768 color space[190,191,203]. The mask created by the threshold color was set to *black and white (B&W)*.
1769 The image was converted to binary by setting *Image Type* to *8-bit*. The stained area was first
1770 delineated by the *Freehand selections* tool, and the *Edit Clear Outside* function was used to
1771 eliminate pixels outside of the selected area. *Analyze Particles* was used to measure the total
1772 stained area. The process was repeated for hematoxylin-stained images to obtain the total

1773 micromass culture area. For neural crest-derived sphere analysis, each well was quantified by
1774 visualization on a ZEISS Axiovert 25 at 10x magnification, and a minimum cell cluster diameter
1775 of 40 µm was used as a cut-off to qualify as a counted sphere. Quantitative results (N=3-6 mouse
1776 embryos from 2-4 dams, unless otherwise mentioned in the Results and/or Figure Legends) for
1777 all counts and measurements are represented by mean ± SEM and were either analyzed by a two-
1778 tailed unpaired t test or a two-way ANOVA with Tukey's post hoc analysis in GraphPad Prism 9
1779 (GraphPad Software). Both sexes were analyzed together by t-test if a sex difference was not
1780 identified. If a sex difference was identified, sexes were analyzed in separate groups by two-way
1781 ANOVA. Statistical significance was defined as $p<0.05$.
1782
1783

Figure 1

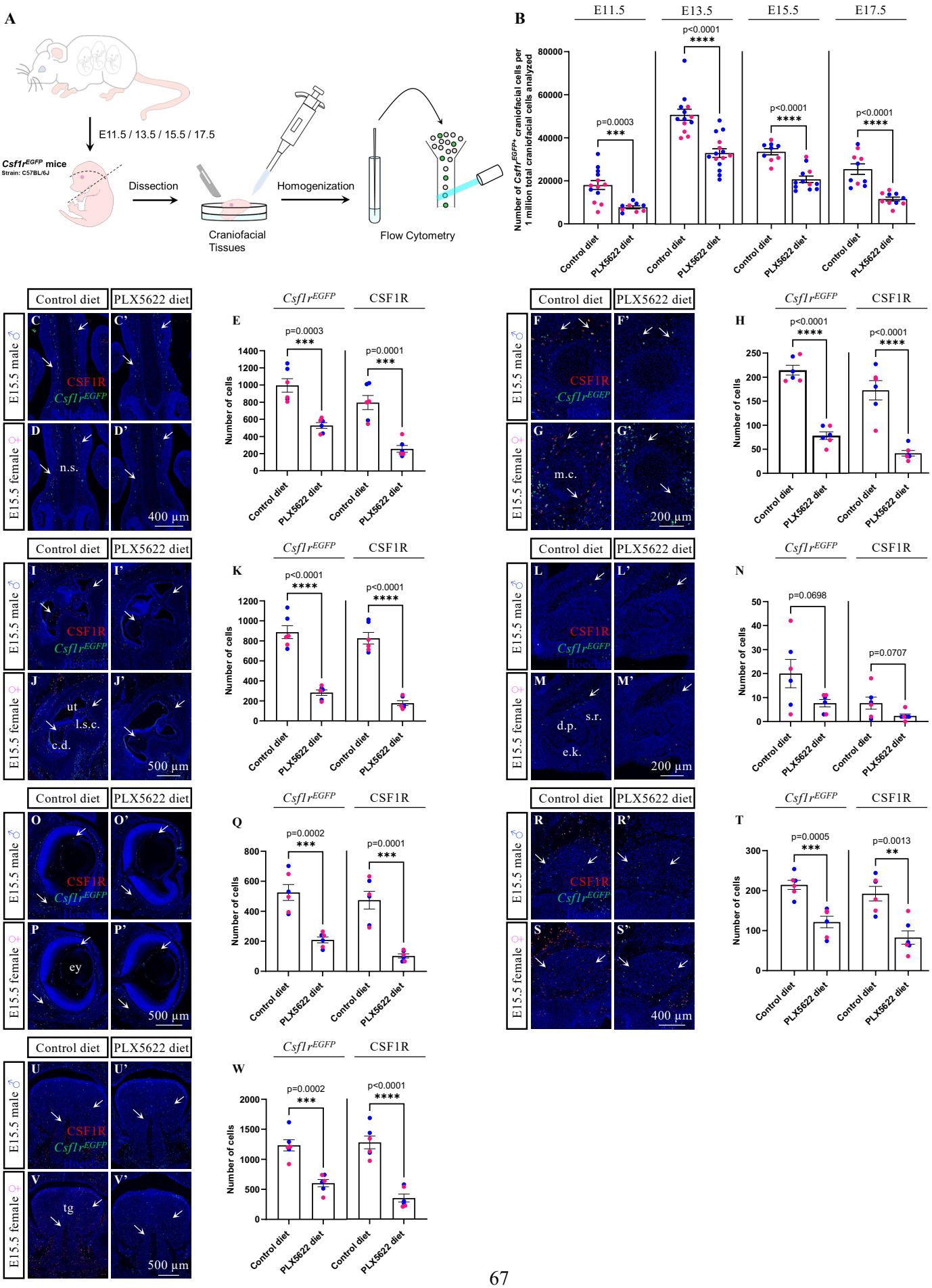
A
E11.5 / 13.5 / 15.5 / 17.5
Csf1r^EGFP mice
Strain: C57BL/6J
Dissection
Craniofacial Tissues
Homogenization
Flow Cytometry
B
E11.5
E13.5
E15.5
E17.5
Number of Csf1r^EGFP+ craniofacial cells per 1 million total craniofacial cells analyzed
p=0.0003
p<0.0001
Control diet
PLX5622 diet
Control diet
PLX5622 diet
Control diet
PLX5622 diet
Control diet
PLX5622 diet
E15.5 male
E15.5 female
CSF1R
Csf1r^EGFP
Hoechst
n.s.
m.c.
ut
l.s.c.
c.d.
s.r.
d.p.
e.k.
ey
tg
400 µm
200 µm
500 µm
Csf1r^EGFP
CSF1R
Number of cells
p=0.0003
p=0.0001
p<0.0001
p=0.0698
p=0.0707
p=0.0002
p=0.0005
p=0.0013

Figure 2

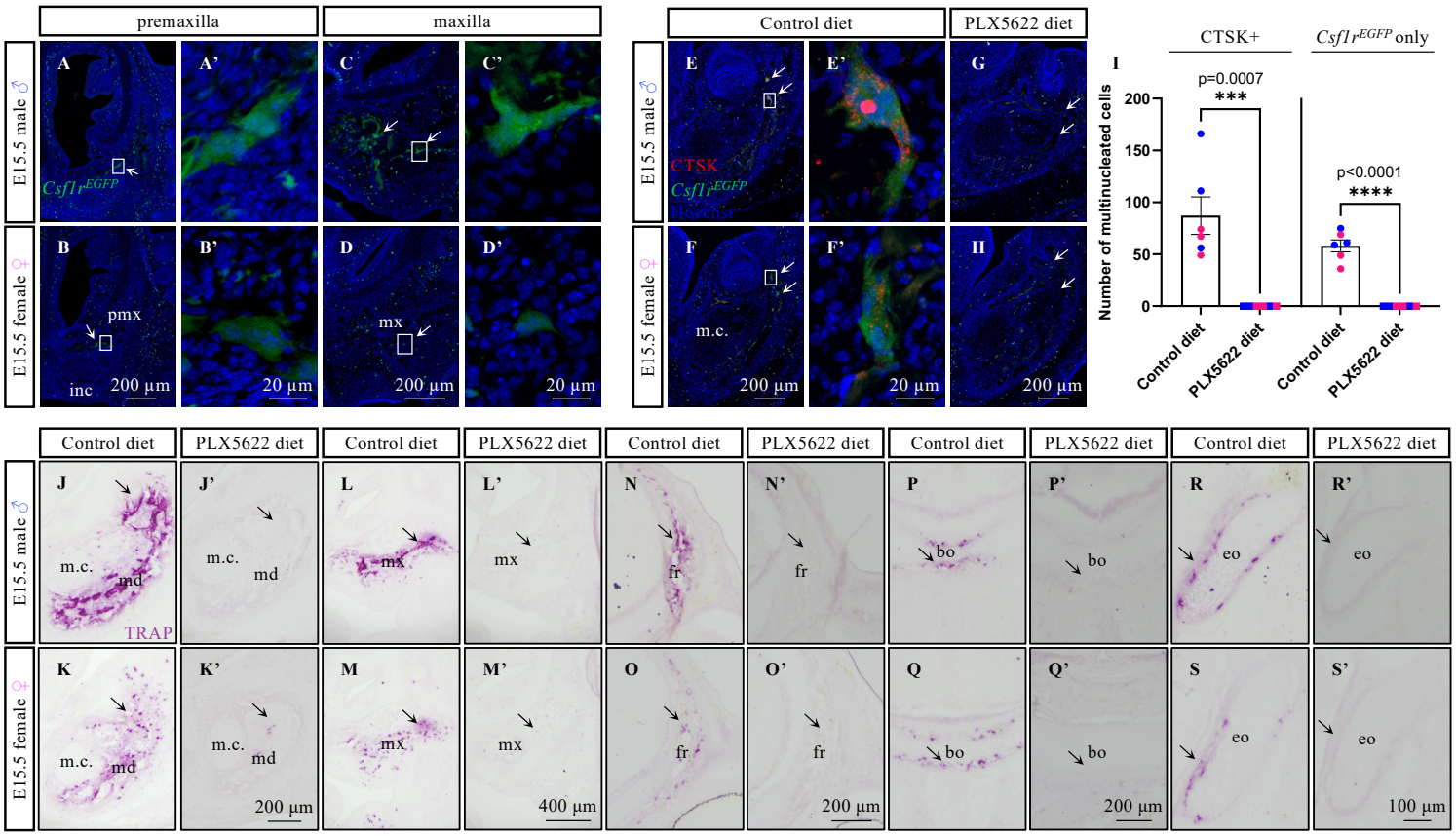
premaxilla
maxilla
Control diet
PLX5622 diet
E15.5 male ♂
E15.5 female ♀
A
A'
C
C'
E
E'
G
B
B'
D
D'
F
F'
H
Csf1r EGFP
CTSK
Hoechst
pmx
mx
inc
m.c.
200 µm
20 µm
I
CTSK+
Csf1r EGFP only
p=0.0007
***
p<0.0001
****
Number of multinucleated cells
200
150
100
50
0
Control diet
PLX5622 diet
J
J'
L
L'
N
N'
P
P'
R
R'
K
K'
M
M'
O
O'
Q
Q'
S
S'
TRAP
md
fr
bo
eo
400 µm
100 µm

Figure 3

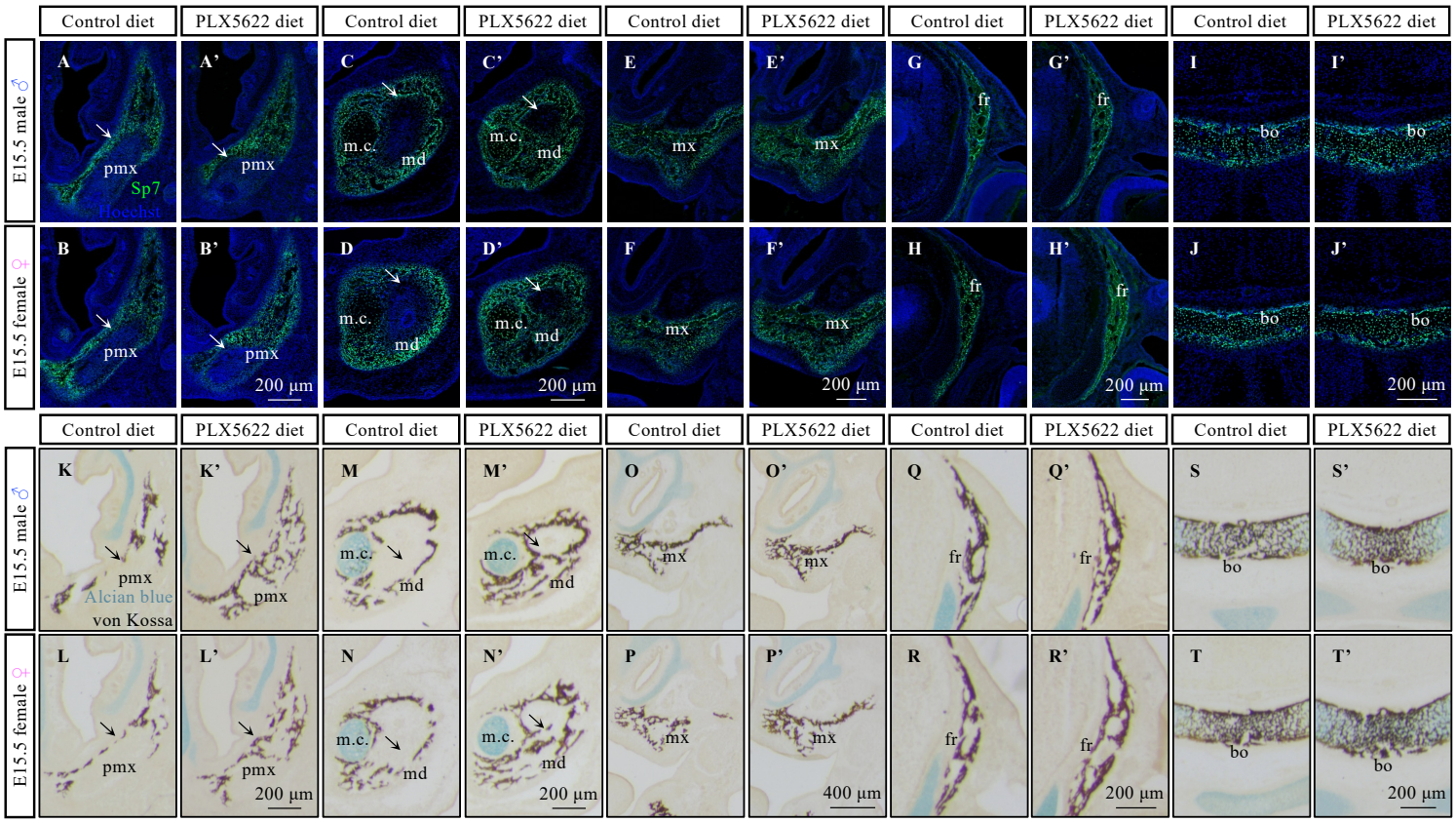
Control diet
PLX5622 diet
E15.5 male ♂
E15.5 female ♀
A
A'
B
B'
C
C'
D
D'
E
E'
F
F'
G
G'
H
H'
I
I'
J
J'
pmx
Sp7
Hoechst
m.c.
md
mx
fr
bo
200 µm
K
K'
L
L'
M
M'
N
N'
O
O'
P
P'
Q
Q'
R
R'
S
S'
T
T'
Alcian blue
von Kossa
400 µm

Figure 4

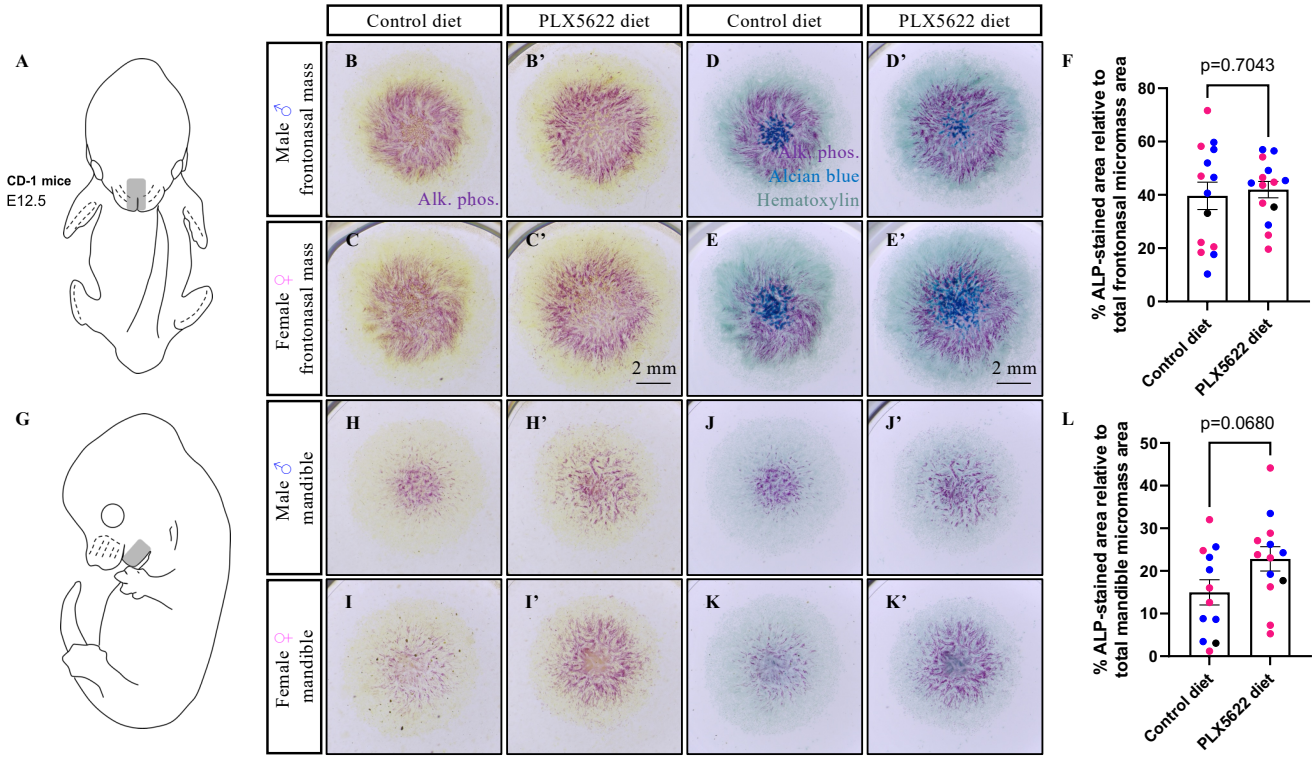
A
CD-1 mice
E12.5
Control diet
PLX5622 diet
Control diet
PLX5622 diet
Male ♂ frontonasal mass
Female ♀ frontonasal mass
Male ♂ mandible
Female ♀ mandible
B
B'
D
D'
C
C'
E
E'
H
H'
J
J'
I
I'
K
K'
Alk. phos.
Alk. phos.
Alcian blue
Hematoxylin
2 mm
2 mm
G
F
p=0.7043
% ALP-stained area relative to total frontonasal micromass area
80
60
40
20
0
Control diet
PLX5622 diet
L
p=0.0680
% ALP-stained area relative to total mandible micromass area
50
40
30
20
10
0
Control diet
PLX5622 diet

Figure 5

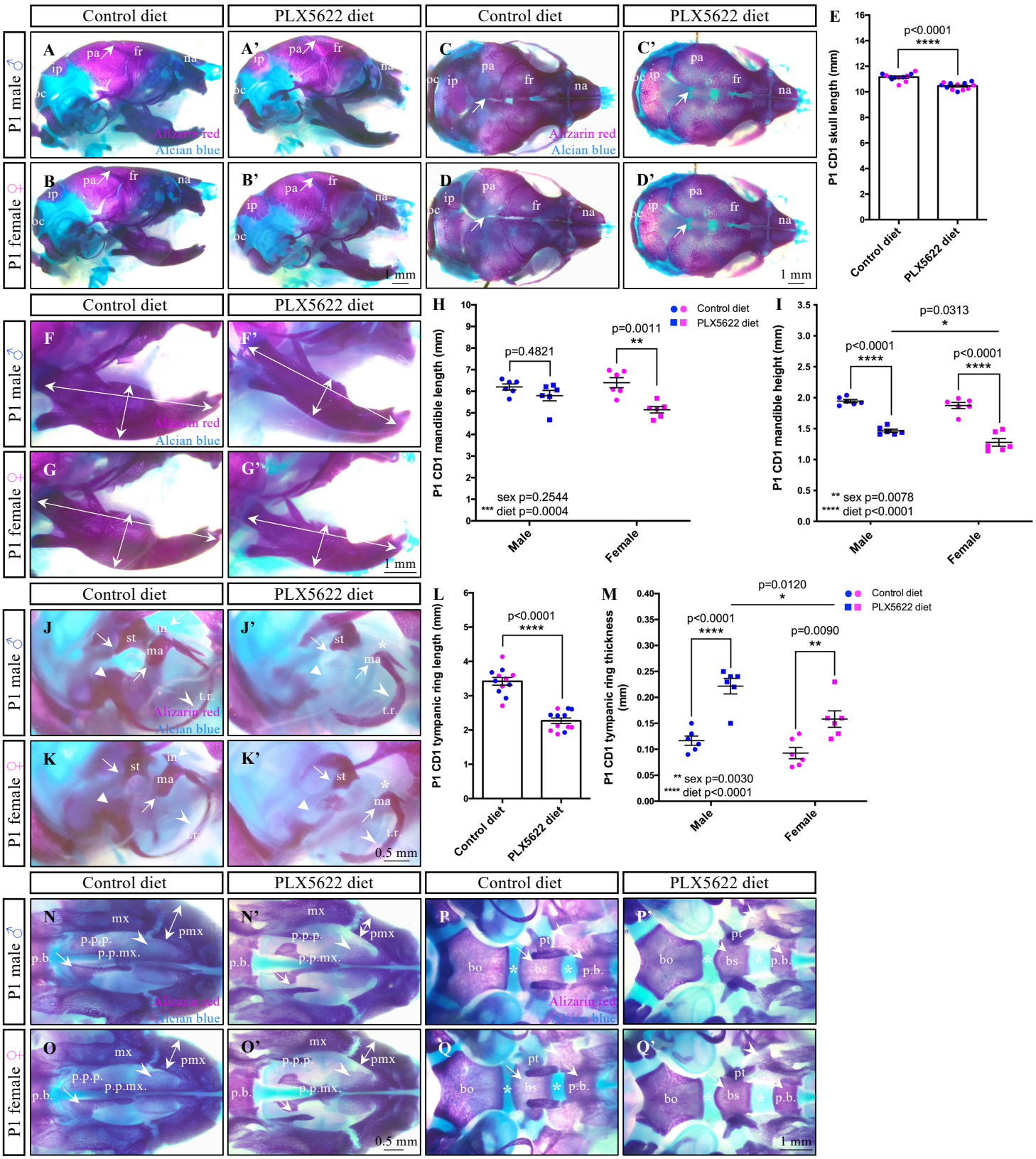
Control diet
PLX5622 diet
P1 male
P1 female
Alizarin red
Alcian blue
1 mm
0.5 mm
pa
fr
na
ip
oc
st
in
ma
t.r.
mx
pmx
p.p.p.
p.p.mx.
p.b.
bo
bs
pt
E
P1 CD1 skull length (mm)
p<0.0001
****
H
P1 CD1 mandible length (mm)
p=0.4821
p=0.0011
**
sex p=0.2544
*** diet p=0.0004
Male
Female
I
P1 CD1 mandible height (mm)
p=0.0313
*
p<0.0001
****
** sex p=0.0078
**** diet p<0.0001
L
P1 CD1 tympanic ring length (mm)
M
P1 CD1 tympanic ring thickness (mm)
p=0.0120
p=0.0090
** sex p=0.0030
**** diet p<0.0001

Figure 6

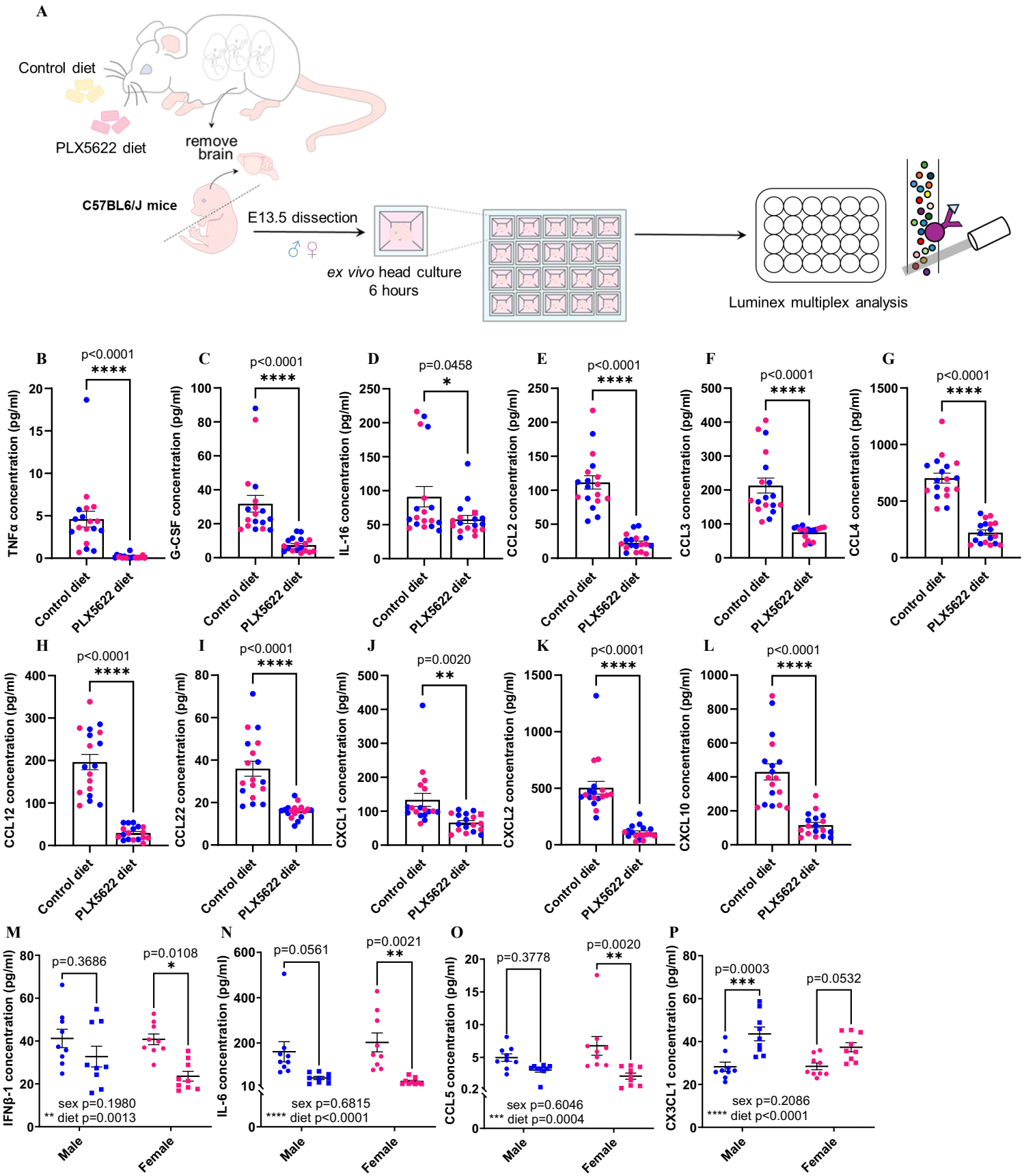
A
Control diet
PLX5622 diet
remove brain
C57BL6/J mice
E13.5 dissection
♂ ♀
ex vivo head culture 6 hours
Luminex multiplex analysis
B
TNFα concentration (pg/ml)
p<0.0001
****
C
G-CSF concentration (pg/ml)
p<0.0001
****
D
IL-16 concentration (pg/ml)
p=0.0458
*
E
CCL2 concentration (pg/ml)
p<0.0001
****
F
CCL3 concentration (pg/ml)
p<0.0001
****
G
CCL4 concentration (pg/ml)
p<0.0001
****
H
CCL12 concentration (pg/ml)
p<0.0001
****
I
CCL22 concentration (pg/ml)
p<0.0001
****
J
CXCL1 concentration (pg/ml)
p=0.0020
**
K
CXCL2 concentration (pg/ml)
p<0.0001
****
L
CXCL10 concentration (pg/ml)
p<0.0001
****
Control diet
PLX5622 diet
M
IFNβ-1 concentration (pg/ml)
p=0.3686
p=0.0108
*
sex p=0.1980
** diet p=0.0013
N
IL-6 concentration (pg/ml)
p=0.0561
p=0.0021
**
sex p=0.6815
**** diet p<0.0001
O
CCL5 concentration (pg/ml)
p=0.3778
p=0.0020
**
sex p=0.6046
*** diet p=0.0004
P
CX3CL1 concentration (pg/ml)
p=0.0003
***
p=0.0532
sex p=0.2086
**** diet p<0.0001
Male
Female

Figure 7

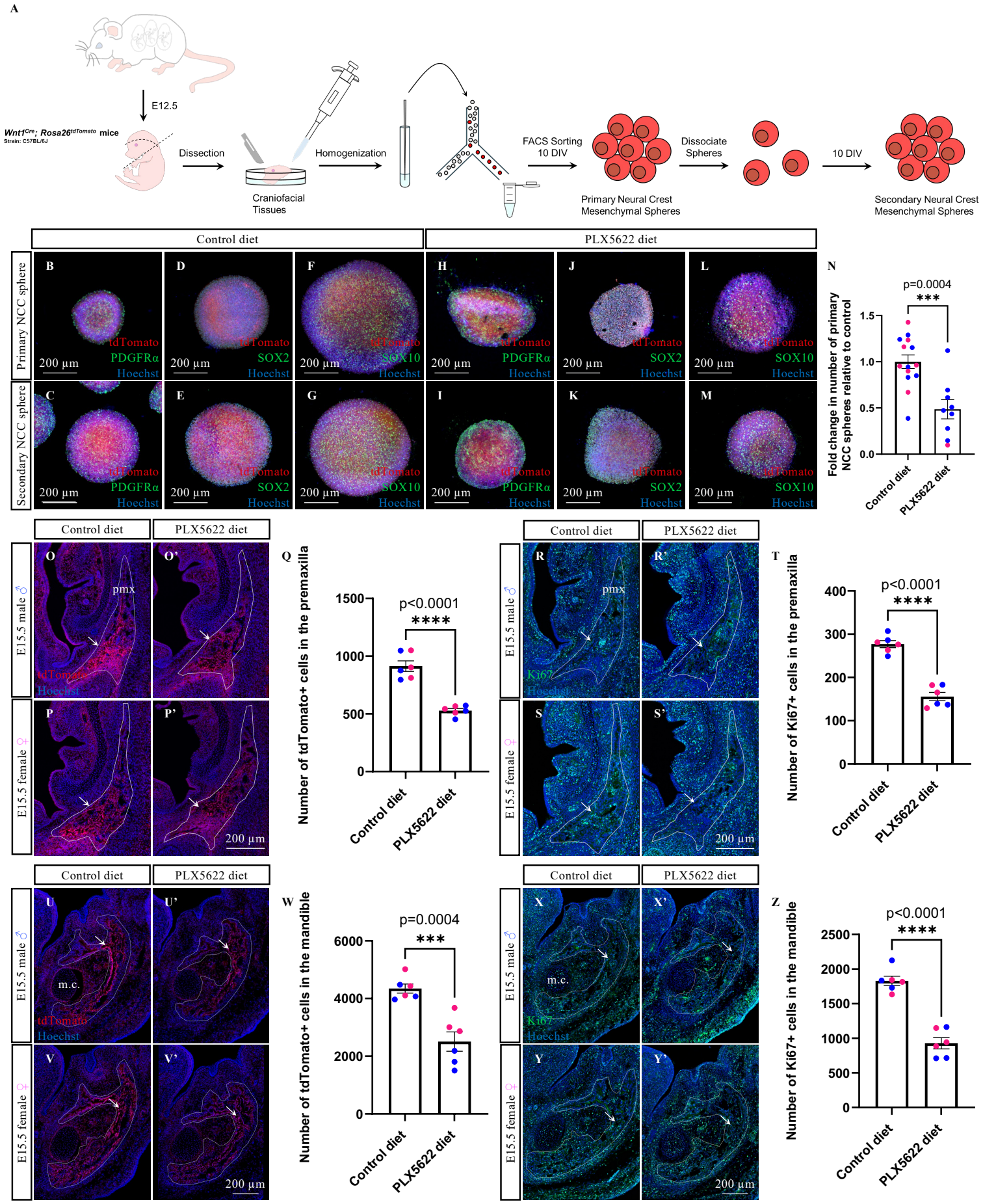
A
E12.5
Wnt1Cre; Rosa26tdTomato mice
Strain: C57BL/6J
Dissection
Craniofacial Tissues
Homogenization
FACS Sorting 10 DIV
Primary Neural Crest Mesenchymal Spheres
Dissociate Spheres
10 DIV
Secondary Neural Crest Mesenchymal Spheres
Control diet
PLX5622 diet
Primary NCC sphere
Secondary NCC sphere
tdTomato
PDGFRα
SOX2
SOX10
Hoechst
200 µm
N
p=0.0004
***
Fold change in number of primary NCC spheres relative to control
Control diet
PLX5622 diet
E15.5 male
E15.5 female
pmx
Q
p<0.0001
****
Number of tdTomato+ cells in the premaxilla
R
S
Ki67
T
Number of Ki67+ cells in the premaxilla
m.c.
W
p=0.0004
***
Number of tdTomato+ cells in the mandible
X
Y
Z
p<0.0001
****
Number of Ki67+ cells in the mandible